Available online at www.sciencedirect.com
ScienceDirect
Journal of Computational Physics 227 (2008) 4955–4976
JOURNAL OF COMPUTATIONAL PHYSICS
www.elsevier.com/locate/jcp

A comparative study of the LBE and GKS methods for 2D near incompressible laminar flows

Zhaoli Guo [a], Hongwei Liu [b], Li-Shi Luo [c,*], Kun Xu [b]

[a] National Laboratory of Coal Combustion, Huazhong University of Science and Technology, Wuhan 430074, China
[b] Department of Mathematics, Hong Kong University of Science and Technology, Clear Water Bay, Kowloon, Hong Kong
[c] Department of Mathematics and Statistics, Center for Computational Sciences, Old Dominion University, Norfolk, VA 23529, USA

Received 18 January 2007; received in revised form 19 December 2007; accepted 15 January 2008
Available online 26 January 2008

Abstract

We compare the lattice Boltzmann equation (LBE) and the gas-kinetic scheme (GKS) applied to 2D incompressible laminar flows. Although both methods are derived from the Boltzmann equation thus share a common kinetic origin, numerically they are rather different. The LBE is a finite difference method, while the GKS is a finite-volume one. In addition, the LBE is valid for near incompressible flows with low-Mach number restriction $Ma < 0.3$, while the GKS is valid for fully compressible flows. In this study, we use the generalized lattice Boltzmann equation (GLBE) with multiple-relaxation-time (MRT) collision model, which overcomes all the apparent defects in the popular lattice BGK equation. We use both the LBE and GKS methods to simulate the flow past a square block symmetrically placed in a 2D channel with the Reynolds number Re between 10 and 300. The LBE and GKS results are validated against the well-resolved results obtained using finite-volume method. Our results show that both the LBE and GKS yield quantitatively similar results for laminar flow simulations, and agree well with existing ones, provided that sufficient grid resolution is given. For 2D problems, the LBE is about 10 and 3 times faster than the GKS for steady and unsteady flow calculations, respectively, while the GKS uses less memory. We also observe that the GKS method is much more robust and stable for under-resolved cases due to its upwinding nature and interpolations used in calculating fluxes.

Keywords: Lattice Boltzmann equation; Gas-kinetic scheme; Linearized Boltzmann equation; Incompressible flows; 2D flow past a square in a channel

1. Introduction

In general, kinetic methods for computational fluid dynamics (CFD) are derived from the Boltzmann equation, as opposed to conventional CFD methods based on direct discretizations of the Navier–Stokes equations. Two distinctive features of kinetic methods immediately appear. First, kinetic methods can include

* Corresponding author. Tel.: +1 757 683 5295; fax: +1 757 683 3885.
E-mail addresses: zlguo@hust.edu.cn (Z. Guo), lluo@odu.edu (L.-S. Luo), makxu@ust.hk (K. Xu).

0021-9991/$ - see front matter © 2008 Elsevier Inc. All rights reserved.
doi:10.1016/j.jcp.2008.01.024

extended hydrodynamics beyond the validity regime of the Navier–Stokes equations, because they are based on kinetic theory. It is known that the Boltzmann equation provides the theoretical connection between hydrodynamics and the underlying microscopic physics. Kinetic methods are often called mesoscopic methods for they act between the macroscopic conservation laws and their corresponding microscopic dynamics. And second, the Boltzmann equation is a first-order integro-partial-differential equation with a linear advection term, while the Navier–Stokes equation is a second-order partial-differential equation with a nonlinear advection term. The nonlinearity in the Boltzmann equation resides in its collision term, which is local. This feature may lead to some computational advantages [1]. For these reasons, kinetic methods have attracted some interest recently. Due to their mesoscopic nature, kinetic methods are particularly appealing in modeling and simulations of complex fluids (cf. [2] and references therein).

There are a number of kinetic or mesoscopic methods, such as the lattice gas cellular automata (LGCA), the lattice Boltzmann equation (LBE), the gas-kinetic schemes (GKS), the smoothed particle hydrodynamics (SPH), and the dissipative particle dynamics (DPD). Among these methods, the LBE and GKS methods are specifically designed as numerical methods for CFD: the former is only valid for near incompressible flows while the latter is for fully compressible flows. Both methods have been applied to simulate viscous flows [3,4], heat transfer problems [5,6], shallow water equations [7], multiphase [8–11] and multi-component [12–17] flows, magnetohydrodynamics [18–20], and microflows [21–24]. Besides their common connections to the Boltzmann equation, the LBE and GKS methods are quite different in many ways. First of all, the LBE is a finite difference (FD) method while the GKS is a finite-volume (FV) one. Second, the LBE is a system evolving on the discrete phase space $\Gamma^* := (\delta x\mathbb{Z}^d, \{\boldsymbol{c}_i\})$ and in discrete time $t_n \in \delta t\mathbb{N}_0 := \delta t\{0, 1, 2, \ldots\}$, where $\delta x\mathbb{Z}^d$ is a d-dimension lattice space with a lattice spacing δx, $\{\boldsymbol{c}_i | i = 0, 1, 2, \ldots, N\}$ is a finite discrete velocity set, and δt is the time step size. In the LBE, the phase space $\Gamma := (\boldsymbol{x}, \boldsymbol{\xi})$ and time t are discretized in such way that for any lattice point $\boldsymbol{x}_j \in \delta x\mathbb{Z}^d$, $\boldsymbol{x}_j + \boldsymbol{c}_i\delta t \in \delta x\mathbb{Z}^d$ for all $\boldsymbol{c}_i \in \{\boldsymbol{c}_i\}$. In contrast, the particle velocity space $\boldsymbol{\xi}$ remains continuous in the GKS, and the space $\boldsymbol{x}$ and time t are discretized independently. However, the grid spacing Δx and time step size Δt in the GKS must satisfy certain stability criteria. Finally and most importantly, in the LBE, the Maxwellian equilibrium distribution function is approximated by its low-order Taylor expansion about zero flow velocity. This approximation limits the LBE method to near incompressible flows with low-Mach number restriction $Ma < 0.3$. The GKS method uses the Maxwellian equilibrium distribution function without any approximation, and it is valid for fully compressible flows.

A comparison between the GKS and LBE methods has been made previously [25]. However, the previous study [25] has a very limited scope. First, the GKS was compared with the lattice Bhatnagar–Gross–Krook [26] (BGK) equation or LBGK model [27,28], which has some severe defects leading to numerical instability and inaccurate boundary conditions [29,30]. Second, the previous study is limited to steady internal flow (the 2D lid-driven cavity flow). And third, only the numerical accuracy of both methods are compared in the previous study, but the numerical stability and computational efficiency of these two methods were not investigated.

The present work is motivated to provide a more thorough comparative study of the LBE and GKS methods for simulations of near incompressible flows. The present work differs from the previous study in several aspects. First of all, instead of the popular LBGK equation [27,28], we shall use the generalized lattice Boltzmann equation (GLBE) with multiple-relaxation-time (MRT) collision model [31]. The GLBE or MRT-LBE can overcome *all* the apparent defects in the LBGK equation. Second, test case used in this work is an open flow involving boundary conditions different from the ones in internal flows. Finally, we will investigate in detail the numerical accuracy, stability and efficiency of both the LBE and GKS methods for low-Mach number laminar flows. We will also validate both the LBE and GKS methods by comparing our results with the existing ones obtained by other well-established methods.

The remaining part of this paper is organized as follows. We provide first a succinct discussion on kinetic theory, especially on the linearized Boltzmann equation, and then the formulations of the GKS and LBE methods in Section 2. We discuss the test flow problem in detail in Section 3. The test case we choose is the 2D flow past a square block symmetrically placed in a channel [32]. We discuss two methods to evaluate hydrodynamic forces: the pressure-tensor integration method and the momentum-exchange method, used in the GKS and LBE simulations, respectively. We report the numerical results with the Reynolds number Re between 10 and 300 in Section 4, which include both steady and unsteady flows. We compare velocity fields,

the wake length behind the square, and the drag and lift coefficients obtained by the GKS and LBE methods. Our results are validated by the results obtained by a well resolved FV simulation [32]. Finally, we conclude the paper with a summary in Section 5.

2. The numerical methods: GKS and LBE

2.1. The linearized Boltzmann equation

The Boltzmann equation is the evolution equation for the single particle velocity distribution function f in phase space $\Gamma := (\boldsymbol{x}, \boldsymbol{\xi})$:

$$D_t f = \Omega(f, f), \quad D_t := \partial_t + \boldsymbol{\xi} \cdot \nabla, \quad \Omega := \int \mathrm{d}\boldsymbol{\xi}_2 \, \mathrm{d}\epsilon \, \mathrm{d}\theta B(\theta, V)[f_1' f_2' - f_1 f_2], \tag{1}$$

where $V := \|\boldsymbol{\xi}_1 - \boldsymbol{\xi}_2\|$, and Ω is the collision operator satisfying the following local conservation laws:

$$\int \phi_\alpha \Omega(f, f) \mathrm{d}\boldsymbol{\xi} = 0, \quad \phi_\alpha \in \{1, \boldsymbol{\xi}, \xi^2/2\}, \tag{2}$$

ϕ_α's are the summational invariants for monatomic gases. Detailed description of the Boltzmann equation can be found in standard textbooks on kinetic theory (e.g. [33,34]).

When the system is at equilibrium, i.e. $f = f^{(0)}$, the collision term vanishes, and the equilibrium $f^{(0)}$ is a local Maxwellian depending on the (macroscopic) hydrodynamic variables, the density ρ, flow velocity $\boldsymbol{u}$, and temperature T, as follows:

$$f^{(0)}(\boldsymbol{\xi}; \rho, \boldsymbol{u}, T) = \frac{\rho}{(2\pi RT)^{d/2}} \exp\left[-\frac{(\boldsymbol{\xi} - \boldsymbol{u})^2}{2RT}\right], \tag{3}$$

where d is the spatial dimension, and R is the gas constant. The hydrodynamic variables are also the (conserved) moments of f and its equilibrium $f^{(0)}$:

$$\rho = \int f \, \mathrm{d}\boldsymbol{\xi} = \int f^{(0)} \, \mathrm{d}\boldsymbol{\xi}, \tag{4a}$$

$$\rho \boldsymbol{u} = \int \boldsymbol{\xi} f \, \mathrm{d}\boldsymbol{\xi} = \int \boldsymbol{\xi} f^{(0)} \, \mathrm{d}\boldsymbol{\xi}, \tag{4b}$$

$$\rho e = \frac{1}{2}\rho(dRT + \boldsymbol{u} \cdot \boldsymbol{u}) = \frac{1}{2}\int \boldsymbol{\xi} \cdot \boldsymbol{\xi} f \, \mathrm{d}\boldsymbol{\xi} = \frac{1}{2}\int \boldsymbol{\xi} \cdot \boldsymbol{\xi} f^{(0)} \, \mathrm{d}\boldsymbol{\xi}, \tag{4c}$$

where e is the specific total energy for monatomic gases.

Because of the insensitivity of hydrodynamics to the details of the underlying microscopic physics and for the sake of computational efficiency, we only use the linearized Boltzmann equation to derive kinetic schemes:

$$D_t f = f^{(0)} L(g), \quad L(g) := \int \mathrm{d}\boldsymbol{\xi}_2 \, \mathrm{d}\epsilon \, \mathrm{d}\theta B(\theta, V) f_2^{(0)} [g_1' + g_2' - g_1 - g_2], \tag{5}$$

where $f = f^{(0)}(1 + g)$. For Maxwell molecules, $B(\theta, V) = B(\theta)$, then the eigenfunctions $\{\psi_i\}$ of the linearized collision operator L are Sonine polynomials in polar coordinates [33,34], or generalized Hermite polynomials in Cartesian coordinates [35,34], with constant eigenvalues $\{\omega_i\}$. The function g (and f) may be expanded in the complete eigenfunction set $\{\psi_i\}$, therefore:

$$g = \sum_{i=0}^{\infty} a_i \psi_i, \quad L(g) = \sum_{i=1}^{\infty} a_i \omega_i \psi_i. \tag{6}$$

Based on the Gross–Jackson procedure [36,34], which mutilates the spectrum of L by representing all eigenvalues ω_i for $i \geqslant N$ by the single value ω_N, a host of models can be constructed as follows:

$$L_N(g) = \sum_{i=1}^{N-1} a_i \omega_i \phi_i - \omega_N \sum_{i=N}^{\infty} a_i \psi_i = \sum_{i=1}^{N-1} a_i(\omega_i + \omega_N)\psi_i - \omega_N g. \tag{7}$$

Therefore, the linearized Boltzmann equation is modeled by the following equation with $(N-5)$ parameters:

$$D_t f = f^{(0)} \sum_{i=1}^{N-1} a_i(\omega_i + \omega_N)\psi_i - \omega_N[f - f^{(0)}]. \tag{8}$$

Because $a_i = 0$ for $i = 1$–4, corresponding to the collisional invariants, hence the choice of $N = 5$ and $\omega_N = 1/\lambda$ lead to the Bhatnagar–Gross–Krook (BGK) model [34]:

$$D_t f = -\frac{1}{\lambda}[f - f^{(0)}], \tag{9}$$

where the relaxation-time λ is the sole parameter determining the transport coefficients for the model as follows:

$$\mu = \rho v = \lambda \rho R T, \tag{10a}$$

$$\kappa = \frac{d+2}{2}\lambda \rho R^2 T = c_p \mu, \tag{10b}$$

where μ and v are the dynamic and kinematic viscosities, respectively, κ is the thermal conductivity, and $c_p = R(d+2)/2$ is the heat capacity at constant pressure. Obviously, the Prandtl number $Pr := c_p\mu/\kappa = 1$ for the BGK model, and this is a notable deficiency, which can be overcome by introducing one more relaxation parameter into the model.

The BGK model equation (9) admits the following formal solution:

$$f(\boldsymbol{x}, \boldsymbol{\xi}, t) = \mathrm{e}^{-(t-t_0)/\lambda} f(\boldsymbol{x}_0, \boldsymbol{\xi}, t_0) + \frac{1}{\lambda}\int_{t_0}^{t} [f^{(0)}(\boldsymbol{x}', \boldsymbol{\xi}, t')\mathrm{e}^{-(t-t')/\lambda}]\mathrm{d}t', \tag{11}$$

where $\boldsymbol{x}_0 = \boldsymbol{x} - (t - t_0)\boldsymbol{\xi}$ and $\boldsymbol{x}' = \boldsymbol{x} - (t - t')\boldsymbol{\xi}$. It has been recognized that both the lattice BGK model and the gas-kinetic scheme (GKS) are constructed from the above formal solution of the BGK equation [37,38]. The LBE is a finite-difference approximation of the incompressible Navier–Stokes equations [39], while the GKS is a finite-volume approximation of the fully compressible Navier–Stokes equations. In LBE, the continuous velocity space $\boldsymbol{\xi}$ is approximated by a small set of discrete velocities $\{\boldsymbol{c}_i\}$ and the Maxwellian distribution function $f^{(0)}$ is approximated by its second-order Taylor expansion in terms of the flow velocity $\boldsymbol{u}$ about $\boldsymbol{u} = 0$ [37,38]. Neither of these approximations are used in the GKS. In the GKS, the first-order nonequilibrium distribution is computed by $f^{(1)} = -\lambda D_t f^{(0)}$. The fluxes are computed by interpolations from the cell centers to cell boundaries.

2.2. Gas-kinetic scheme

The gas-kinetic scheme (GKS) is a finite-volume (FV) scheme based on the BGK equation (9). The hydrodynamic equations can be written in terms of the conserved variables $\{\Phi_\alpha\}$ and the corresponding fluxes $\{\boldsymbol{J}_\alpha\}$:

$$\partial_t \Phi_\alpha + \nabla \cdot \boldsymbol{J}_\alpha = 0, \tag{12a}$$

$$\Phi_\alpha = \int \phi_\alpha f \,\mathrm{d}\boldsymbol{\xi} \in \{\rho, \rho\boldsymbol{u}, \rho e\}, \quad \boldsymbol{J}_\alpha = \int \boldsymbol{\xi}\phi_\alpha f \,\mathrm{d}\boldsymbol{\xi}, \tag{12b}$$

where $\phi_\alpha \in \{1, \boldsymbol{\xi}, \xi^2/2\}$ are the collisional invariants. To formulate an FV scheme, Eq. (12a) is integrated over a cell of volume V_i and boundary ∂V_i:

$$\partial_t \int_{V_i} \Phi_\alpha \,\mathrm{d}V + \int_{\partial V_i} \hat{\boldsymbol{n}} \cdot \boldsymbol{J}_\alpha \,\mathrm{d}s = 0, \tag{13}$$

where $\hat{\boldsymbol{n}}$ is the unit out-normal vector of the cell surface. The time averaging of Eq. (13) over one time step leads to:

$$\overline{\Phi}_\alpha^{n+1} - \overline{\Phi}_\alpha^{n} + \frac{1}{V_i}\int_{t_n}^{t_{n+1}} \mathrm{d}t \int_{\partial V_i} \mathrm{d}s\, \hat{\boldsymbol{n}} \cdot \boldsymbol{J}_\alpha = 0, \tag{14}$$

where $\overline{\Phi}^n_\alpha := \overline{\Phi}_\alpha(t_n)$ and $\overline{\Phi}_\alpha$ denotes the volume average of Φ_α:

$$\overline{\Phi}_\alpha := \frac{1}{V_i}\int_{V_i} \Phi_\alpha \mathrm{d}V.$$

The key feature that distinguished the GKS from all other FV schemes based on direct discretizations of the Navier–Stokes equations lies in the construction of the fluxes at cell interfaces. In the GKS, the fluxes are evaluated from the distribution function f based on Eq. (11), as opposed to various numerical differentiation techniques. For *smooth* flows without shocks, f can be approximated at the cell interface $\boldsymbol{x}_{i+1/2}$, as depicted in Fig. 1, as the following [25]:

$$\begin{aligned} f(\boldsymbol{x}_{i+1/2},\boldsymbol{\xi},t) &= [1+(t-t_n)\partial_t]f(\boldsymbol{x}_{i+1/2},\boldsymbol{\xi},t_n) \approx [(1-\lambda D_t)+(t-t_n)\partial_t]f^{(0)}(\boldsymbol{x}_{i+1/2},\boldsymbol{\xi},t_n) \\ &= [1-\lambda(A+\boldsymbol{\xi}\cdot\boldsymbol{a})+(t-t_n)A]f^{(0)}(\boldsymbol{x}_{i+1/2},\boldsymbol{\xi},t_n), \end{aligned} \tag{15}$$

where $\boldsymbol{a} = \nabla \ln f^{(0)}$ and $A = \partial_t \ln f^{(0)}$ in 3D can be explicitly given:

$$\boldsymbol{a} = \nabla \ln \rho + \left(\frac{c^2}{2RT} - \frac{3}{2}\right)\nabla \ln T + \frac{1}{RT} c_\alpha \nabla u_\alpha, \tag{16a}$$

$$A = -\boldsymbol{\xi}\cdot\boldsymbol{a} + \left(\frac{c^2}{2RT} - \frac{5}{2}\right)\boldsymbol{c}\cdot\nabla \ln T + \frac{1}{RT}\left(\boldsymbol{cc} - \frac{1}{3}c^2\mathsf{I}\right) : \nabla\boldsymbol{u}, \tag{16b}$$

where the convention for summation over the repeated indexes is used and I is the 3×3 identity matrix. In Eq. (15), two approximations have been applied. First, f is approximated by its second-order Chapman–Enskog expansion in the context of the BGK equation, i.e. $f \approx (1-\lambda D_t)f^{(0)}$. And second approximation is that $\partial_t f \approx \partial_t f^{(0)}$, which is consistent with the second-order Chapman–Enskog expansion and includes only the first-order derivatives of the hydrodynamic variables ρ, $\boldsymbol{u}$ and T. To obtain Eqs. (16) for $\boldsymbol{a}$ and A, the Euler equations must be used to substitute the time derivatives of ρ, $\boldsymbol{u}$ and T by their spatial gradients.

To compute f at the cell boundary $\boldsymbol{x}_{i+1/2}$, one needs $f^{(0)}$ and its derivatives at $\boldsymbol{x}_{i+1/2}$, which in turn are given by the hydrodynamic variables and their derivatives at $\boldsymbol{x}_{i+1/2}$. The hydrodynamic variables and their derivatives at $x_{i+1/2}$ are obtained by interpolations of their averaged values at cell centers $\{x_i\}$ about the cell boundary $x_{i+1/2}$. Consequently, the accuracy of the interpolations determines the accuracy of the GKS method. Once the value of f is known at the cell boundary $\boldsymbol{x}_{i+1/2}$, the fluxes can be easily computed. It should be emphasized that Eq. (15) assumes no shocks, hence no discontinuities, in the flow. Otherwise, discontinuities of hydrodynamic variables at cell interfaces should be explicitly considered in $f^{(0)}$, and approximation of f at cell boundaries must be derived from Eq. (11) with consideration of the discontinuities [4]. In the present work, symmetric two-point interpolations are used to compute the hydrodynamic variables ρ, $\boldsymbol{u}$ and T at the cell boundary $\boldsymbol{x}_{i+1/2}$, i.e. the values of ρ, $\boldsymbol{u}$ and T at $\boldsymbol{x}_{i+1/2}$ are the averages of their values at x_i and x_{i+1}. The same two points are also used to compute the spatial derivatives of ρ, $\boldsymbol{u}$ and T at $\boldsymbol{x}_{i+1/2}$ [25].

For isothermal flows, the temperature T is a constant, the parameters $\boldsymbol{a}$ and A in Eq. (15) reduce to:

$$\boldsymbol{a} = \nabla \ln \rho + \frac{1}{RT} c_\alpha \nabla u_\alpha \tag{17a}$$

$$A = -\boldsymbol{\xi}\cdot\boldsymbol{a} + \frac{1}{RT}(\boldsymbol{cc} - RT\mathsf{I}) : \nabla\boldsymbol{u}. \tag{17b}$$

Because $\boldsymbol{a}$ and A are given in terms of the primitive variables $(\rho, \boldsymbol{u}, T)$, but they must be computed in terms of the conserved variables $(\rho, \rho\boldsymbol{u}, \rho e)$. This can be accomplished by directly using the Jacobian between the primitive and conserved variables or by using the compatibility conditions that:

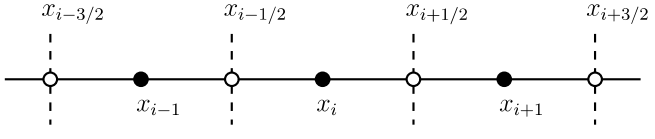

Fig. 1. Schematic for the cell centers (•) and cell interfaces (○) in the GKS.

$$\int f^{(n)}\phi_\alpha \mathrm{d}\boldsymbol{\xi} = 0, \quad n \geqslant 1, \ \phi_\alpha \in \{1, \boldsymbol{\xi}, \xi^2/2\}, \tag{18}$$

where $f^{(n)}$ for $n \geqslant 1$ is the nth order nonequilibrium distribution function in the Chapman–Enskog expansion of f. Because $f^{(1)} = -\lambda D_t f^{(0)}$ for the BGK equation, therefore

$$\int \boldsymbol{\xi}\cdot\boldsymbol{a} f^{(0)}\phi_\alpha \mathrm{d}\boldsymbol{\xi} = -\int A f^{(0)}\phi_\alpha \mathrm{d}\boldsymbol{\xi}. \tag{19}$$

It can be shown that this compatibility condition is automatically satisfied by $\boldsymbol{a}$ and A given by Eqs. (16) for fully compressible flows, or Eqs. (17) for isothermal flows.

With $\boldsymbol{a}$ and A at cell boundaries determined by the hydrodynamic variables $(\rho, \boldsymbol{u}, T)$ at the cell centers $\{\boldsymbol{x}_i\}$, the distribution function f can be computed at cell boundaries $\{\boldsymbol{x}_{i\pm1/2}\}$, hence the total fluxes across the cell interfaces in the time interval $[t_n, t_{n+1}]$ can be easily computed. Then the conserved variables $(\rho, \rho\boldsymbol{u}, \rho e)$ can be updated according to Eq. (14). It should be noted that for isothermal near-incompressible flows studied in the present work, the temperature is a constant thus the equation for the internal energy is eliminated in the GKS method.

As an explicit numerical scheme, the time step Δt in the GKS is dictated by flow characteristics. For high-Reynolds number flows in which the convection term is dominant, and the time step Δt is determined by the Courant–Friedrichs–Lewy (CFL) condition:

$$\Delta t = \eta \frac{\Delta x}{(|\boldsymbol{u}|_{\max} + c_s)}, \quad 0 \leqslant \eta \leqslant 1,$$

where η is the CFL number, Δx is the minimum cell size, $|\boldsymbol{u}|_{\max}$ is the maximum of the velocity, and $c_s = \sqrt{RT}$ is the speed of sound. For low-Reynolds number flows, the viscous term is dominant, thus the time step is determined by the following condition:

$$\Delta t \leqslant \frac{(\Delta x)^2}{2^d \nu}.$$

Consequently, a unified stability condition can be obtained [40]:

$$\Delta t \leqslant \frac{\eta \Delta x}{(|\boldsymbol{u}| + c_s)(1 + 2/Re^*)}, \tag{20}$$

where $Re^* = |\boldsymbol{u}|\Delta x/\nu$ is the grid Reynolds number. It has been shown that the GKS method is second-order accurate in both space and time [41]. For isothermal flows, the speed of sound c_s is a constant, and the time step size Δt can be determined *a priori* with given values of Δx and η. This practice saves some computational time in the GKS method.

2.3. The generalized lattice Boltzmann equation

The generalized lattice Boltzmann equation (GLBE) with multiple-relaxation-time (MRT) collision model is a fully discrete model based on the linearized Boltzmann equation. The lattice Boltzmann equation can be defined by three key ingredients. First of all, the model evolves on a discrete phase space $\Gamma^* := \{\delta x\mathbb{Z}^d, \{\boldsymbol{c}_i\}\}$ with discrete time $\delta t\mathbb{N}_0 := \delta t\{0, 1, 2, \ldots\}$. The discrete phase space Γ^* consists of a d-dimensional lattice space $\delta x\mathbb{Z}^d$ with a lattice spacing δx and a finite symmetric discrete velocity set $\{\boldsymbol{c}_i | i = 0, 1, N\} = -\{\boldsymbol{c}_i\}$, where $\boldsymbol{c}_0 = \boldsymbol{0}$, so that:

$$\boldsymbol{x}_j + \boldsymbol{c}_i\delta t \in \delta x\mathbb{Z}^d, \quad \forall \boldsymbol{c}_i \in \{\boldsymbol{c}_i\} \text{ and } \boldsymbol{x}_j \in \delta x\mathbb{Z}^d.$$

The particle velocity space $\boldsymbol{\xi}$ is approximated by the discrete velocity set $\{\boldsymbol{c}_i\}$. Second, corresponding to $\{\boldsymbol{c}_i\}$, there is a set of distribution functions $\{f_i\}$ on each grid point $\boldsymbol{x}_j$. The particle transport is modeled by moving of $\{f_i\}$ from one grid point $\boldsymbol{x}_j$ to its neighboring points $\boldsymbol{x}_j + \{\boldsymbol{c}_i\}\delta t$; and the inter-particle collision is modeled by linear relaxation processes to the local Maxwellian. And third, the evolution equation of a lattice Boltzmann model is written in general as the following:

$$\mathbf{f}(\boldsymbol{x}_j + \boldsymbol{c}\delta t, t_{n+1}) - \mathbf{f}(\boldsymbol{x}_j, t_n) = -\mathsf{M}^{-1} \cdot \mathsf{S}\big[\mathbf{m}(\boldsymbol{x}_j, t_n) - \mathbf{m}^{(\mathrm{eq})}(\boldsymbol{x}_j, t_n)\big], \tag{21}$$

where $t_{n+1} := t_n + \delta t$, $\mathbf{f}$ is the $(N+1)$-tuple vector of the discrete distribution functions $\{f_i | i = 0, 1, \ldots, N\}$:

$$\mathbf{f}(\boldsymbol{x}_j + \boldsymbol{c}\delta t, t_n) := (f_0(\boldsymbol{x}_j, t_n), f_1(\boldsymbol{x}_j + \boldsymbol{c}_1\delta t, t_n), \ldots, f_N(\boldsymbol{x}_j + \boldsymbol{c}_N\delta t, t_n))^{\mathsf{T}},$$
$$\mathbf{f}(\boldsymbol{x}_j, t_n) := (f_0(\boldsymbol{x}_j, t_n), f_1(\boldsymbol{x}_j, t_n), \ldots, f_N(\boldsymbol{x}_j, t_n))^{\mathsf{T}},$$

$\mathbf{m}$ and $\mathbf{m}^{(\mathrm{eq})}$ are $(N+1)$-tuple vectors of moments and their equilibria, M is an $(N+1) \times (N+1)$ transformation matrix, so that:

$$\mathbf{m} = \mathsf{M} \cdot \mathbf{f}, \quad \mathbf{f} = \mathsf{M}^{-1} \cdot \mathbf{m}, \tag{22}$$

and S is a non-negative definite $(N+1) \times (N+1)$ diagonal matrix:

$$\mathsf{S} = \mathrm{diag}(s_0, s_1, \ldots, s_N), \quad s_i \geqslant 0, \tag{23}$$

where $\{s_i\}$ are relaxation rates.

The matrix M is so constructed that $\mathsf{M} \cdot \mathsf{M}^{\mathsf{T}}$ is a diagonal matrix. That is, the column vectors $\{\mathbf{e}_i\}$ of M^{T} are mutually orthogonal by construction [31,42,43,5], i.e. $\mathbf{e}_i \cdot \mathbf{e}_j^{\mathsf{T}} = \|\mathbf{e}_i\|\delta_{ij}$. The construction of M is directly related to the finite orthogonal polynomials $\{\varphi_i | i = 0, 1, \ldots, N\}$ on the discrete velocity set $\{\boldsymbol{c}_i\}$. In fact, the jth component of $\mathbf{e}_i$, e_{ij}, is $\varphi_i(\boldsymbol{c}_j)$. The orthogonal polynomials $\{\varphi_i | i = 0, 1, \ldots, N\}$ are analogous to the generalized Hermite polynomials on continuous $\boldsymbol{\xi}$-space, except that $\{\varphi_i\}$ is orthogonal on a discrete velocity set $\{\boldsymbol{c}_i\}$, and has a finite number of polynomials, which is equal to the number of discrete velocities. The equilibria of moments, $\{\mathbf{m}^{(\mathrm{eq})}\}$, are polynomials of conserved variables in the system, which are obtained through Taylor expansion of the Maxwellian about $\boldsymbol{u} = \mathbf{0}$. Because M and $\{\mathbf{m}^{(\mathrm{eq})}\}$ are specifically related to the discrete velocity set $\{\boldsymbol{c}_i\}$, we will provide a concrete example with a specific discrete velocity set $\{\boldsymbol{c}_i\}$.

Eq. (21) presents a very simple evolutionary dynamics: its left-hand-side represents particle transport by simple advection, which only involves data movements from one lattice node $\boldsymbol{x}_j$ to its neighboring nodes $\boldsymbol{x}_j + \boldsymbol{c}_i\delta t$ and is executed in velocity space; and its right-hand-side represents collision process modeled by linear relaxation processes executed in moment space. Thus, the lattice Boltzmann algorithm consists two simple steps: advection and collision and can be written as the following:

$$f_i(\boldsymbol{x}_j + \boldsymbol{c}_i\delta t, t_n + \delta t) - f_i(\boldsymbol{x}_j, t_n) = \sum_k \frac{s_k e_{ki}}{\|\mathbf{e}_k\|}\Big[m_k(\boldsymbol{x}_j, t_n) - m_k^{(\mathrm{eq})}(\boldsymbol{x}_j, t_n)\Big]. \tag{24}$$

The advantage of executing the advection and collision in the velocity space and moment space, respectively, would become apparent later.

In the present work, we confine ourselves to isothermal low-Mach number flows in two dimensions (2D). For this purpose, we can use the nine velocity model in 2D, i.e. the D2Q9 model. The discrete velocities are:

$$\boldsymbol{c}_i = \begin{cases} (0,0)c, & i = 0, \\ (\pm 1, 0)c, \ (0 \pm 1)c, & i = 1\text{–}4, \\ (\pm 1, \pm 1)c, & i = 5\text{–}8, \end{cases} \tag{25}$$

where $c := \delta x/\delta t$. We arrange the moments in the following order:

$$\mathbf{m} := (\rho, e, \varepsilon, j_x, q_x, j_y, q_y, p_{xx}, p_{xy})^{\mathsf{T}}, \tag{26}$$

where $m_0 = \rho$ is the density, $m_1 = e$ is related to the total energy, $m_1 = \varepsilon$ is related to energy square, $(m_3, m_5) := (j_x, j_y) := \rho(u_x, u_y)$ is the flow momentum, $(m_4, m_4) := (q_x, q_y)$ is related to the head flux, and $m_7 = p_{xx}$ and $m_8 = p_{xy}$ are related to the diagonal and off-diagonal components of the stress tensor, respectively. Because we are only interested in isothermal system, the conserved variables are the density and momentum $\boldsymbol{j} := \rho\boldsymbol{u}$:

$$\rho = \sum_i f_i, \quad \rho\boldsymbol{u} = \sum_i \boldsymbol{c}_i f_i. \tag{27}$$

Because the energy is *not* a conserved variable, such LBE models are also called a thermal ones. Accordingly, the equilibrium moments are:

$$m_1^{(\mathrm{eq})} = 3\left(u_x^2 + u_y^2\right) - 2\rho, \quad m_2^{(\mathrm{eq})} = -3\left(u_x^2 + u_y^2\right) + \rho, \tag{28a}$$

$$m_4^{(\mathrm{eq})} = -u_x, \quad m_6^{(\mathrm{eq})} = -u_y, \tag{28b}$$

$$m_7^{(\mathrm{eq})} = u_x^2 - u_y^2, \quad m_8^{(\mathrm{eq})} = u_x u_y. \tag{28c}$$

Note that the equilibria of the conserved moments are equal to themselves. We have made two related approximations in $\{m_i^{(\mathrm{eq})}\}$. First, because we are only interested in low-Mach number flows, the terms higher than u^2 are ignored in the equilibria. And second, for the same reason, terms related to $\delta\rho u$ are also ignored, where $\delta\rho$ is the density fluctuation: $\rho := \rho_0 + \delta\rho$ and $\rho_0 = 1$. In effect, the density is decoupled from the momentum modes so that $\boldsymbol{u} = \sum_i \boldsymbol{c}_i f_i$ instead of Eq. (27). With the ordering of moments specified by Eq. (26), the transform matrix M for the D2Q9 model is given by [42]

$$\mathsf{M} = \begin{pmatrix} e_0^{\mathsf{T}} \\ e_1^{\mathsf{T}} \\ e_2^{\mathsf{T}} \\ e_3^{\mathsf{T}} \\ e_4^{\mathsf{T}} \\ e_5^{\mathsf{T}} \\ e_6^{\mathsf{T}} \\ e_7^{\mathsf{T}} \\ e_8^{\mathsf{T}} \end{pmatrix} = \begin{pmatrix} 1 & 1 & 1 & 1 & 1 & 1 & 1 & 1 & 1 \\ -4 & -1 & -1 & -1 & -1 & 2 & 2 & 2 & 2 \\ 4 & -2 & -2 & -2 & -2 & 1 & 1 & 1 & 1 \\ 0 & 1 & 0 & -1 & 0 & 1 & -1 & -1 & 1 \\ 0 & -2 & 0 & 2 & 0 & 1 & -1 & -1 & 1 \\ 0 & 0 & 1 & 0 & -1 & 1 & 1 & -1 & -1 \\ 0 & 0 & -2 & 0 & 2 & 1 & 1 & -1 & -1 \\ 0 & 1 & -1 & 1 & -1 & 0 & 0 & 0 & 0 \\ 0 & 0 & 0 & 0 & 0 & 1 & -1 & 1 & -1 \end{pmatrix}. \tag{29}$$

With the equilibria given by Eqs. (28), the Navier–Stokes equations can be derived from the MRT-LBE with an equation of state $p = \rho/3$, i.e. the speed of sound is $c_s = 1/\sqrt{3}c$, and the shear and bulk viscosities are given by [42]

$$\nu = \frac{1}{3}\left(\frac{1}{s_7} - \frac{1}{2}\right)c\delta t = \frac{1}{3}\left(\frac{1}{s_8} - \frac{1}{2}\right)c\delta t, \tag{30a}$$

$$\zeta = \frac{1}{6}\left(\frac{1}{s_1} - \frac{1}{2}\right)c\delta t, \quad c := \delta x/\delta t. \tag{30b}$$

If we set $s_i = 1/\tau$, the GLBE (21) reduces to the lattice BGK (LBGK) model [27,28] with the equilibrium distribution function $f_i^{(\mathrm{eq})}$ directly derived from the Taylor expansion of the Maxwellian [37,38]. For the LBGK D2Q9 model, $\zeta = \nu/2 = (\tau - 1/2)/6$. Therefore, the LBGK model is particularly prone to numerical instability due to spurious fluctuations in density and other nonconserved modes, for there is insufficient dissipation for these fluctuations when τ is closed to 1/2. In the GLBE, for those nonconserved moments which have negligible effects to hydrodynamics, the relaxation rates $\{s_i\}$ corresponding to these moments can be optimized to attain optimal linear stability, and this is the flexibility the LBGK equation cannot afford. In addition, the GLBE can adjust the heat conductivity κ independent of the viscosity ν, thus it is not subject to the problem of the Prandtl number $Pr = 1$, which is inherent to the BGK model.

Now, some comments comparing the LBE and GKS are in order here. The lattice Boltzmann equation in general is a discrete moment system aiming to approximate the incompressible Navier–Stokes equations [39]. The simplicity of the LBE leads to its computational efficiency, but also makes it difficult to accurately model the evolution of the higher order moments beyond the hydrodynamics [44]. On the other hand, the gas-kinetic scheme solves the full compressible Navier–Stokes equations within the kinetic framework: the fluxes are evaluated as moments of the distribution function f, which is an approximated solution of the BGK model equation. Depending on how f is approximated, higher order moments beyond the hydrodynamics can be computed [24,45]. In addition, there are other differences. First, in LBE, $c := \delta x/\delta t = 1$. However, this does not mean that the CFL number $\eta = 1$. Because the LBE is always subject to the low-Mach number restriction

$Ma < 0.3$ for near incompressible flows, therefore $\eta = (\|\boldsymbol{u}\|_{\max}/c_s)(\delta t/\delta x) = Ma_{\max} < 0.3$. However, for the low-Reynolds number flows, the LBE is stable and is not subject to the condition of Eq. (20). Second, the LBE model has a non-zero bulk viscosity ζ, which is a numerical artifact due to discretization affecting attenuation of sound waves and can be analyzed [42,5]. While the BGK equation does not have a bulk viscosity due to internal degrees of freedom, it is not clear if the GKS has the same effective bulk viscosity due to numerics as in the LBE, because the analysis of acoustic attenuation has not be carried out for the GKS. It is expected that in small scales close to grid spacing, the LBE and GKS would behave differently. We also note that in the GKS for isothermal flows, only $(d+1)$ flow variables need to be stored, whiles in the LBE, there are $(N+1)$ distribution functions $\{f_i\}$ need to be stored, and $(N+1) \gg (d+1)$. Therefore, the GKS is more memory efficient.

3. Flow past a square block in a channel in 2D

3.1. Flow configuration and boundary conditions

The test case used to quantitatively compare the LBE and GKS methods is the two-dimensional (2D) laminar flow past a square block symmetrically placed in a channel with respect to the channel centerline, as depicted in Fig. 2. The dimension of the block is $D \times D$, and that of the channel is $L \times H$, where L and H are length and height of the channel, respectively. The block located at L_1 from the entrance, and its two sides paralleled to the channel walls. The flow configuration is defined by $L = 50D$, $H = 8D$, and $L_1 = 12.5D$ in the simulations. This flow has been subject to experimental [46] and numerical studies [46–48,32]. It thus can serve as a good test case for our study.

The boundary conditions of the flow are specified as follows [32]. At the entrance, a parabolic velocity profile along x-direction is enforced:

$$u_0(x^* = 0, y^*) = U_{\max}(1 - y^*)(1 + y^*),$$
$$v_0(x^* = 0, y^*) = 0,$$

where $U_{\max}$ is the maximum velocity, and $x^* = 2x/H$ and $y^* = 2y/H$. On the block surfaces and the channel walls, no-slip boundary conditions are applied. At the outlet, the convective boundary conditions are applied to all flow variables [32]:

$$\partial_t \varphi + U_{\max} \partial_x \varphi = 0, \tag{31}$$

where $\varphi = \rho$, ρu and ρv.

In the LBE, the velocity boundary conditions at the entrance and the solid walls are realized by the bounce-back scheme [49–51]:

$$f_i(\boldsymbol{x}_f, t_n + \Delta t) = f_{\bar{i}}^*(\boldsymbol{x}_f, t_n) + 2w_i\rho_f \frac{\boldsymbol{c}_i \cdot \boldsymbol{u}(\boldsymbol{x}_b, t_n)}{c_s^2}, \tag{32}$$

where $\boldsymbol{x}_f$ is the fluid node next to the boundary location $\boldsymbol{x}_b$, and $\rho_f := \rho(\boldsymbol{x}_f, t_n)$. Through the bounce-back scheme, the boundary conditions $\boldsymbol{u} = \boldsymbol{u}_b := \boldsymbol{u}(\boldsymbol{x}_b)$ are attained approximately at $\delta x/2$ beyond $\times_f$ [52,53,29,30]. The superscript "*" denotes the post-collision state, i.e.,

$$\mathbf{f}^*(\boldsymbol{x}_j, t_n) = \mathbf{f}(\boldsymbol{x}_j, t_n) + \mathsf{M}^{-1} \cdot \mathsf{S} \cdot [\mathbf{m}(\boldsymbol{x}_j, t_n) - \mathbf{m}^{(\mathrm{eq})}(\boldsymbol{x}_j, t_n)].$$

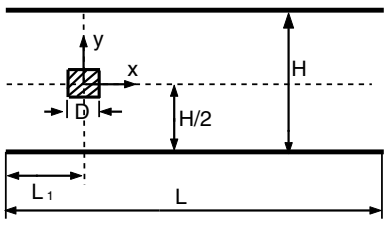

Fig. 2. Schematic of the flow past a square block in a 2D channel.

At the outlet, the incoming distribution function f_i is obtained according to a second-order finite-difference of Eq. (31). Consequently, the density and velocity also obey Eq. (31) since both are the moments of f_i. We note that the specific method to realize the outflow boundary conditions has little effect on the results of interest.

In the GKS, the realization of the velocity boundary condition at the entrance is achieved by the ghost cell method [25]:

$$\rho(x_{-1}) = \rho(x_0), \tag{33a}$$

$$\boldsymbol{j}(x_{-1}) = 2\boldsymbol{j}(x_0) - \boldsymbol{j}(x_1), \quad \boldsymbol{j} := \rho\boldsymbol{u}, \tag{33b}$$

where x_{-1} is the ghost cell, x_1 is the first layer of fluid cell, and x_0 the cell at the entrance. This treatment ensures a second-order accuracy for the velocity boundary conditions. The convective outlet boundary conditions are directly obtained from Eq. (31) by discretizing it using a finite-difference scheme with first-order accuracy in time and second-order accuracy in space. For the solid walls of the channel and the square block, the second-order one-side extrapolation schemes are used to obtain the density and the spatial gradients at the interface in the determination of the surface distribution function f in the GKS.

The bounce-back boundary conditions can also be implemented in GKS:

$$f(\boldsymbol{x}_\mathrm{b}, \boldsymbol{\xi}, t_n) = f(\boldsymbol{x}_\mathrm{b}, -\boldsymbol{\xi}, t_n) + \frac{2\boldsymbol{\xi}\cdot\boldsymbol{u}_\mathrm{b}}{RT_\mathrm{b}} f^{(0)}(\boldsymbol{\xi}; \rho_\mathrm{b}, \boldsymbol{u}_\mathrm{b}, T_\mathrm{b}), \quad \boldsymbol{\xi}\cdot\hat{\boldsymbol{n}} > 0,$$

where $\boldsymbol{\xi}\cdot\hat{\boldsymbol{n}} > 0$, $\hat{\boldsymbol{n}}$ is the out-normal unit vector to the boundary; $\boldsymbol{x}_\mathrm{b}$ is a boundary node; ρ_b, $\boldsymbol{u}_\mathrm{b}$ and T_b are the values at $\boldsymbol{x}_\mathrm{b}$ and time $t = t_n$; and the distribution function $f(\boldsymbol{x}_\mathrm{b}, -\boldsymbol{\xi}, t_n)$ can be constructed according to Eq. (15), where the macroscopic variables are determined using one-side extrapolation.

3.2. Evaluation of the hydrodynamic forces

The force on the square block exerted by the fluid can be obtained by integrating the pressure-tensor along the block surface A,

$$\boldsymbol{F} = -\int_{\partial A} \mathsf{P}\cdot\hat{\boldsymbol{n}}\,\mathrm{d}s = \int_{\partial A} [-p\mathsf{I} + 2\rho\nu\mathsf{S}]\cdot\hat{\boldsymbol{n}}\,\mathrm{d}s, \tag{34}$$

where $S_{\alpha\beta} := \frac{1}{2}(\partial_\alpha u_\beta + \partial_\beta u_\alpha)$ and $\hat{\mathrm{n}}$ is the out-normal unit vector of the boundary ∂A. Note that we have assumed that the flow is nearly incompressible in the second equality. In the GKS, we will employ this *integration* method to evaluate the hydrodynamic force on the block, where the pressure-tensor P on the block surface is evaluated from the time-averaged momentum flux:

$$\mathsf{P} = \frac{1}{\Delta t}\int_{t_n}^{t_n+\Delta t}\int \boldsymbol{\xi}\boldsymbol{\xi} f(\boldsymbol{x}_\mathrm{b}, \boldsymbol{\xi}, t')\mathrm{d}\boldsymbol{\xi}\,\mathrm{d}t', \quad \boldsymbol{x}_\mathrm{b} \in \partial A, \tag{35}$$

where the distribution function at the block surface, $f(\boldsymbol{x}_\mathrm{b}, \boldsymbol{\xi}, t')$, is determined by the boundary conditions previously described. Note that the no-slip boundary conditions at the solid surfaces are applied in Eq. (35).

For the LBE, the hydrodynamic force on the obstacle can also be computed according to Eq. (34). However, a more efficient alternative, i.e. the *momentum-exchange* method [51], can be used. In the bounce-back picture, the momentum of a pre-collision particle moving with velocity $\boldsymbol{c}_i := -\boldsymbol{c}_i$ toward the solid wall will be reversed to $\boldsymbol{c}_i$, and the net change of its momentum is

$$\Delta\boldsymbol{j}_i = \boldsymbol{c}_i f_i(\boldsymbol{x}_\mathrm{f}, t_n + \Delta t) - \boldsymbol{c}_i f_{\bar{i}}^*(\boldsymbol{x}_\mathrm{f}, t_n) = 2\boldsymbol{c}_i f_{\bar{i}}^*(\boldsymbol{x}_\mathrm{f}, t_n),$$

then the total force exerted on the solid due to this collision is approximately:

$$\boldsymbol{F}_i(\boldsymbol{x}_\mathrm{b}, t_n + \Delta t/2) \approx \frac{\Delta\boldsymbol{j}_i}{\Delta t}, \quad \boldsymbol{F} := \sum_i \boldsymbol{F}_i.$$

Consequently, the total hydrodynamic force on the block can be obtained by integrating $\boldsymbol{F}(\boldsymbol{x}_\mathrm{b})$ over its boundary defined by $\{\boldsymbol{x}_\mathrm{b}\}$. It has shown that for the LBE method, the momentum-exchange and the integration methods yield comparable results, but the former is more efficient computationally than the latter [54].

4. Numerical results

Initially, the flow velocity is that of the fully developed channel flow, i.e. $u(x,y) = u_{\text{in}}(y)$, and the block appears impulsively at $t_0 = 0$. The Reynolds number of the flow is $Re = DU_{\max}/\nu$. It is known that then the Reynolds number is below the critical Reynolds number $Re_c \approx 60$, the flow is steady. Beyond the critical Reynolds number Re_c, the flow becomes unsteady.

Two uniform meshes are used in the simulations: a coarse mesh of 501×81, i.e. $D = 10$, and a finer one of 1001×161, i.e. $D = 20$. Since both the LBE and GKS methods are compressible methods, the Mach number, $Ma = U_{\max}/\sqrt{RT}$, is set to be 0.1 so that the compressible effect is negligible. Because we are interested in isothermal flow, the temperature T is a constant, which is chosen to be $RT = 1/3$ in the units of $c = \delta x/\delta t = 1$.

The relaxation parameters in the MRT-LBE are set as follows: for the conserved variables, $s_0 = s_3 = s_5 = 0$; For the shear modes, $s_7 = s_8$ are determined by Eq. (30a) according to the value of the Reynolds number. Other relaxation parameters in the MRT-LBE are: $s_1 = 1.1$, $s_2 = 1.0$ and $s_4 = s_6 = 1.2$. The choice of these relaxation parameters is based on two considerations: (a) separation between the hydrodynamic and kinetic modes, and (b) numerical stability [42]. The bulk viscosity $\zeta = (s_2 - 1/2)/6 = 1/12$. In the GKS, we set the CFL number $\eta = 0.4$ unless otherwise stated.

In addition to the velocity field, the drag and lift coefficients will also be measured and compared with existing results:

$$C_D = \frac{F_x}{\frac{1}{2}\bar{\rho}U_{\max}^2 D}, \quad C_{\text{L}} = \frac{F_y}{\frac{1}{2}\bar{\rho}U_{\max}^2 D}, \tag{36}$$

where $\bar{\rho}$ is the mean fluid density, F_x and F_y are the streamwise and normal components of the hydrodynamic force $\boldsymbol{F}$, respectively, which are computed by the integration method of Eq. (34) for the GKS, and by the momentum-exchange method for the LBE.

4.1. Steady flow

Since both the LBE and GKS are explicit time-marching methods, a large number of time steps are required to reach a steady-state. In our computations, the working criterion of steady-state is set to be

$$\frac{\sum_i \|\boldsymbol{u}(\boldsymbol{x}_i, t_n) - \boldsymbol{u}(\boldsymbol{x}_i, t_n - 1000\delta t)\|^2}{\sum_i \|\boldsymbol{u}(\boldsymbol{x}_i, t)\|} < 10^{-6}. \tag{37}$$

The steady flow over a square block is characterized by a pair of symmetric stationary recirculating eddies behind the block. The wake length L_r is a function of Re which can be approximated by a linear function [32]:

$$\frac{L_r}{D} \approx -0.065 + 0.0554Re, \quad \text{for } 5 < Re < 60. \tag{38}$$

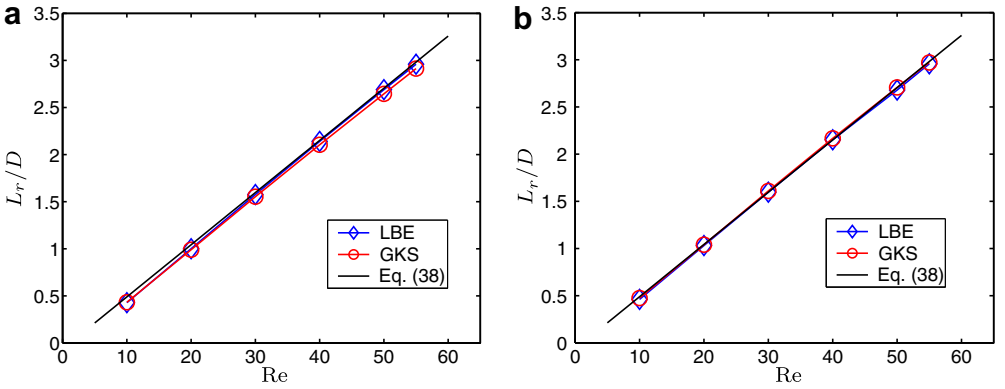

Fig. 3. The Reynolds number dependence of the recirculating wake length L_r for steady flow, $Ma = 0.1$: (a) coarse mesh of 501×81 and (b) fine mesh of 1001×161.

The wake length L_r is measured from the numerical results obtained from both the LBE and GKS methods when a steady-state is attained.

Fig. 3 shows the Reynolds number dependence of L_r. The results obtained by both the LBE and GKS methods fit very well the linear relation of Eq. (38) between L_r and Re. The LBE results agree well with the empirical relationship (38) with both coarse and fine meshes, while the GKS results slightly under-predicts the wake lengths with the coarse mesh, however, the GKS results with the fine mesh agree very well with Eq. (38).

The velocity fields predicted by both the LBE and GKS methods are also studied. Figs. 4 and 5 present various velocity profiles at $Re = 30.0$ and 50.0, respectively, with the coarse mesh of 501×81 ($D = 10\delta x$). In both cases, the velocity profiles obtained by the LBE and GKS are in excellent agreement. The L^2-norm

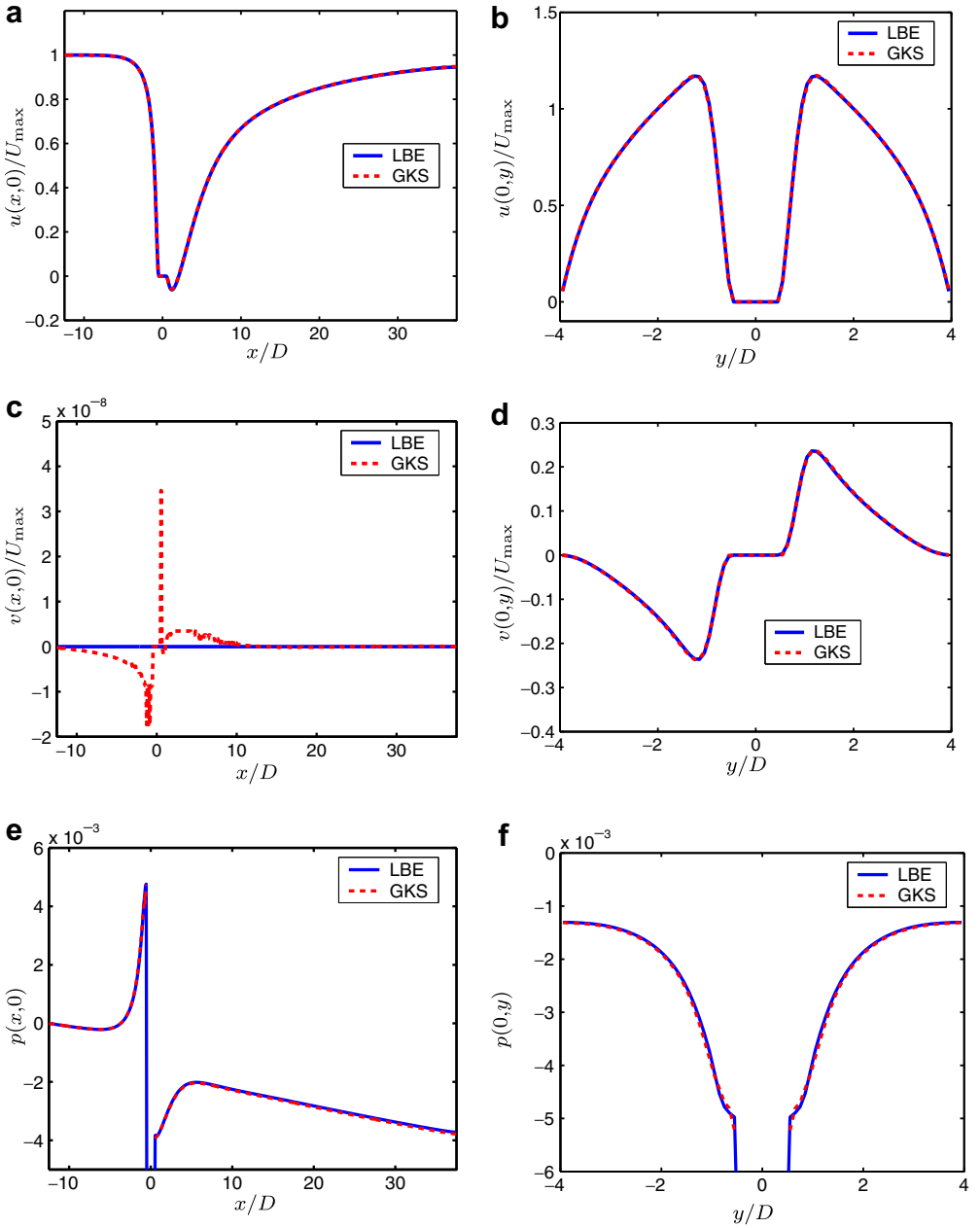

Fig. 4. Velocity profiles at $Re = 30.0$ with the coarse mesh size of 501×81 and $Ma = 0.1$. (a) $u(x,0)$; (b) $u(0,y)$; (c) $v(x,0)$; (d) $v(0,y)$; (e) $p(x,0)$; (f) $p(0,y)$.

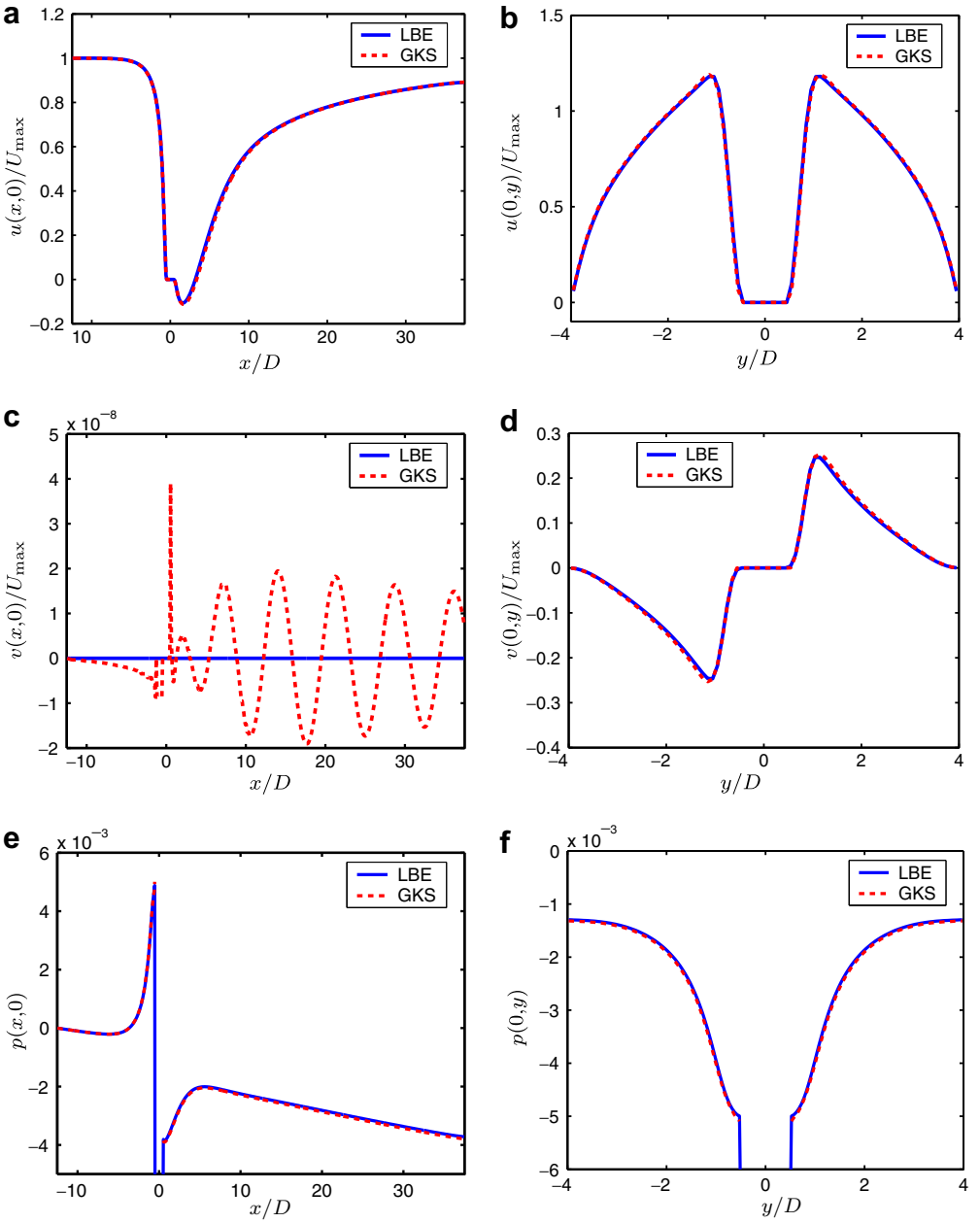

Fig. 5. Same as Fig. 4 at $Re = 50.0$.

difference among the velocity fields $\boldsymbol{u}(\boldsymbol{x}_i, t_n)$ obtained by the LBE and GKS with the coarse mesh is well under 1%: 0.36% and 0.42% for $Re = 30.0$ and 50.0, respectively. While the y-component of velocity along the channel center $v(x, 0)$ obtained from the LBE is zero within the machine accuracy, we note that $v(x, y = 0)$ obtained by the GKS exhibits some oscillations of small amplitudes ($\sim 10^{-8}$), which should be zero since the flow is symmetric about $y = 0$. The oscillation may be due to the different interpolations used for the cells inside the flow domain and those at the solid boundaries. The velocity profiles on the fine mesh are indistinguishable from those on the coarse one for $u(x, 0)$, $u(0, y)$, and $v(0, y)$; although for $v(x, 0)$, some small oscillations are still observed for the GKS results (not shown). This indicates that with the coarse mesh the results are already grid-size independent for $Re = 30.0$ and 50.0.

To demonstrate the convergence behavior for the steady-state calculations, we compute the L^2-norm error of the velocity field:

$$E_2(\boldsymbol{u}) = \sqrt{\frac{\sum_i \|\boldsymbol{u}(\boldsymbol{x}_i) - \boldsymbol{u}^*(\boldsymbol{x}_i)\|^2}{\sum_i \|\boldsymbol{u}^*(\boldsymbol{x}_i)\|^2}}, \tag{39}$$

where the reference solution $\boldsymbol{u}^*$ is the one obtained with Richardson extrapolation. The results shown in Fig. 6 clearly indicates that both the GKS and LBE methods are second-order accurate in space. The least-square fitted slopes from $E_2(u)$ and $E_2(v)$ are 2.1569 and 1.9996, respectively, for the LBE, and 1.9975 and 2.0090, respectively, for the GKS.

In the steady flow regime, the lift force is zero due to the flow symmetry. The drag force, however, varies depending on Re. A comparison of the drag coefficient obtained by the LBE and GKS methods is shown in Fig. 7, together with the results obtained by the finite-volume (FV) method [32], which used a 560×340 non-uniform mesh. We observe that both the LBE and GKS results agree well with the FV data on both the coarse and fine meshes.

Fig. 8 shows the convergence of the drag coefficient C_D and the wake length L_r at $Re = 30.0$ and $Ma = 0.1$. The size of the block D varies from $6\delta x$ to $18\delta x$, i.e. the mesh size $L \times H$ varies from 301×49 to 901×145. Clearly, both C_D and L_r obtained by the LBE and L_r obtained by the GKS show a second-order accuracy. The drag coefficient C_D obtained from the GKS has some interesting nonlinear behavior: for coarse meshes, the

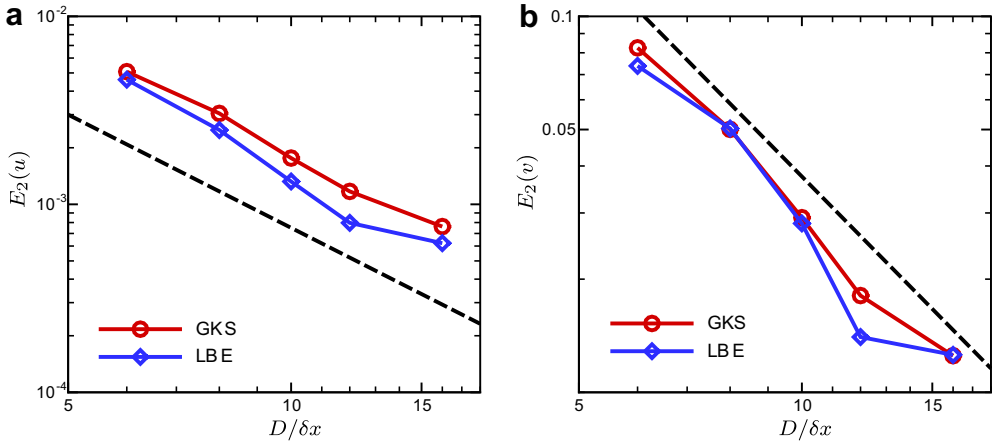

Fig. 6. L^2-norm error of velocity fields at $Re = 30.0$ and $Ma = 0.1$: (a) $E_2(u)$ and (b) $E_2(v)$. The slope of the dashed lines is -2.

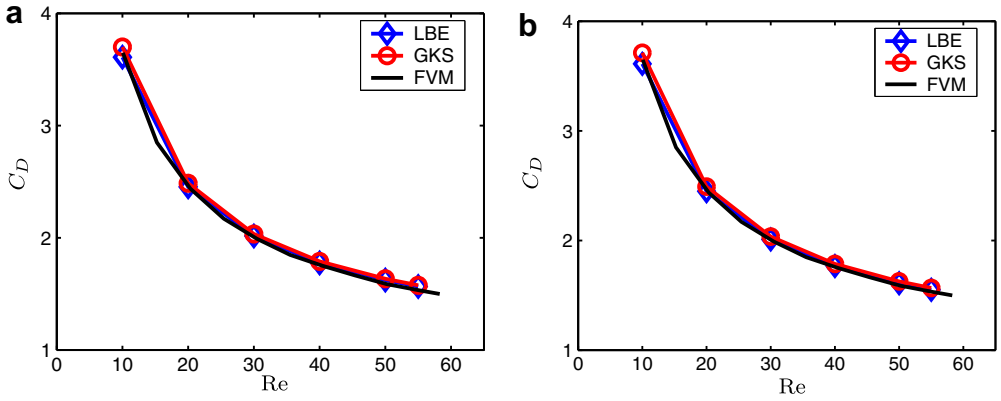

Fig. 7. The Reynolds number dependence of the drag coefficient C_D with $Ma = 0.1$ and two difference mesh sizes: (a) coarse mesh of 501×81 and (b) fine mesh of 1001×161. The finite-volume method (FVM) results are taken from Ref. [32].

error of C_D increases as the mesh refines. The error of C_D eventually reaches to a slope about -2 with finer meshes. This behavior is due to the nonlinear nature of the error in the GKS [55].

Fig. 9 shows the Mach number dependence of C_D and L_r at $Re = 30.0$. For Ma between 0.05 and 0.3, the LBE results have much weaker dependence on Ma than the GKS ones. For both C_D and L_r, the LBE results vary only about 1.0%, while the GKS results vary about 5.0%. This is expected because the compressibility is reduced in the LBE approximation [56], while it is fully retained in the GKS.

Although the LBE and GKS methods have similar capability in the prediction of the fluid behavior, they are considerably different in terms of the computational efficiency. On the coarse mesh, the averaged CPU times the LBE and GKS methods are 1.7×10^{-2} and 5.4×10^{-2} seconds per unit time, respectively, and on the fine mesh, the times are 7.0×10^{-2} and 23.0×10^{-2} s, respectively. Thus, the LBE is about three times faster than the GKS on each node per iteration. In addition, the number of time steps to reach a steady-state is different in the two methods. The LBE method takes less time steps to reach the steady-state criterion of Eq. (37) in this case. In Table 1, the CPU times required to reach a steady-state with the criterion of Eq. (37) are give for a number of different Re values on the two meshes. As shown, the LBE is about one order of magnitude faster than the GKS for steady-state calculations.

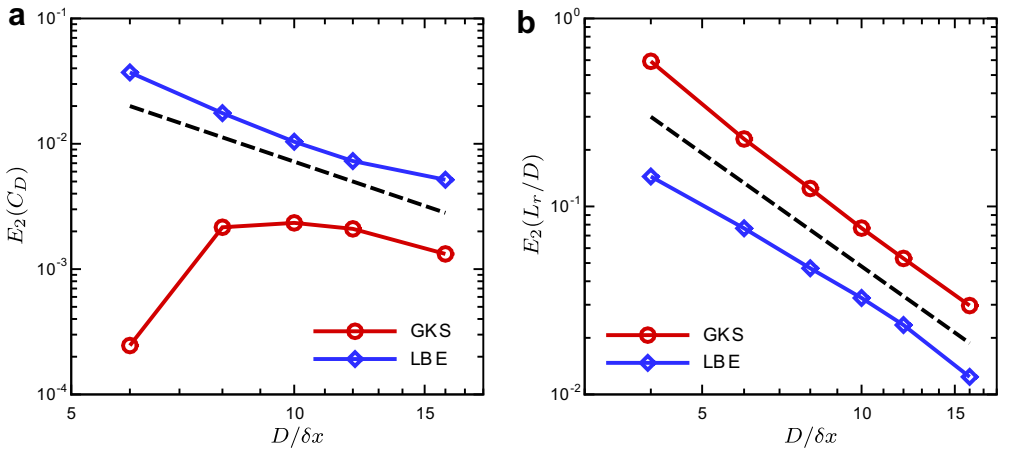

Fig. 8. L^2-norm error of (a) C_D and (b) L_r at $Re = 30.0$ and $Ma = 0.1$. The slop of the dash lines is -2.

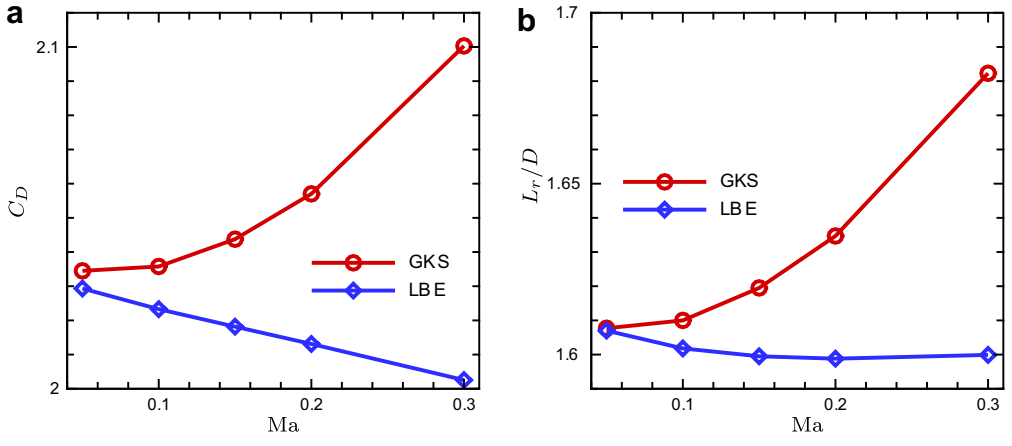

Fig. 9. The Mach number dependence of (a) C_D and (b) L_r/D at $Re = 30.0$ and mesh size 1001×161.

Table 1
CPU time to attain the steady-state using the LBE and GKS methods

		Re					
		10	20	30	40	50	55
Coarse mesh (s)	LBE	259.8	307.6	383.8	444.6	486.0	512.4
	GKS	1676.0	2540.0	3709.0	4022.0	5070.0	5787.0
Fine mesh (s)	LBE	2188	2462	2799	2892	3724	3786
	GKS	10,678	20,560	30,694	33,554	40,618	44,511

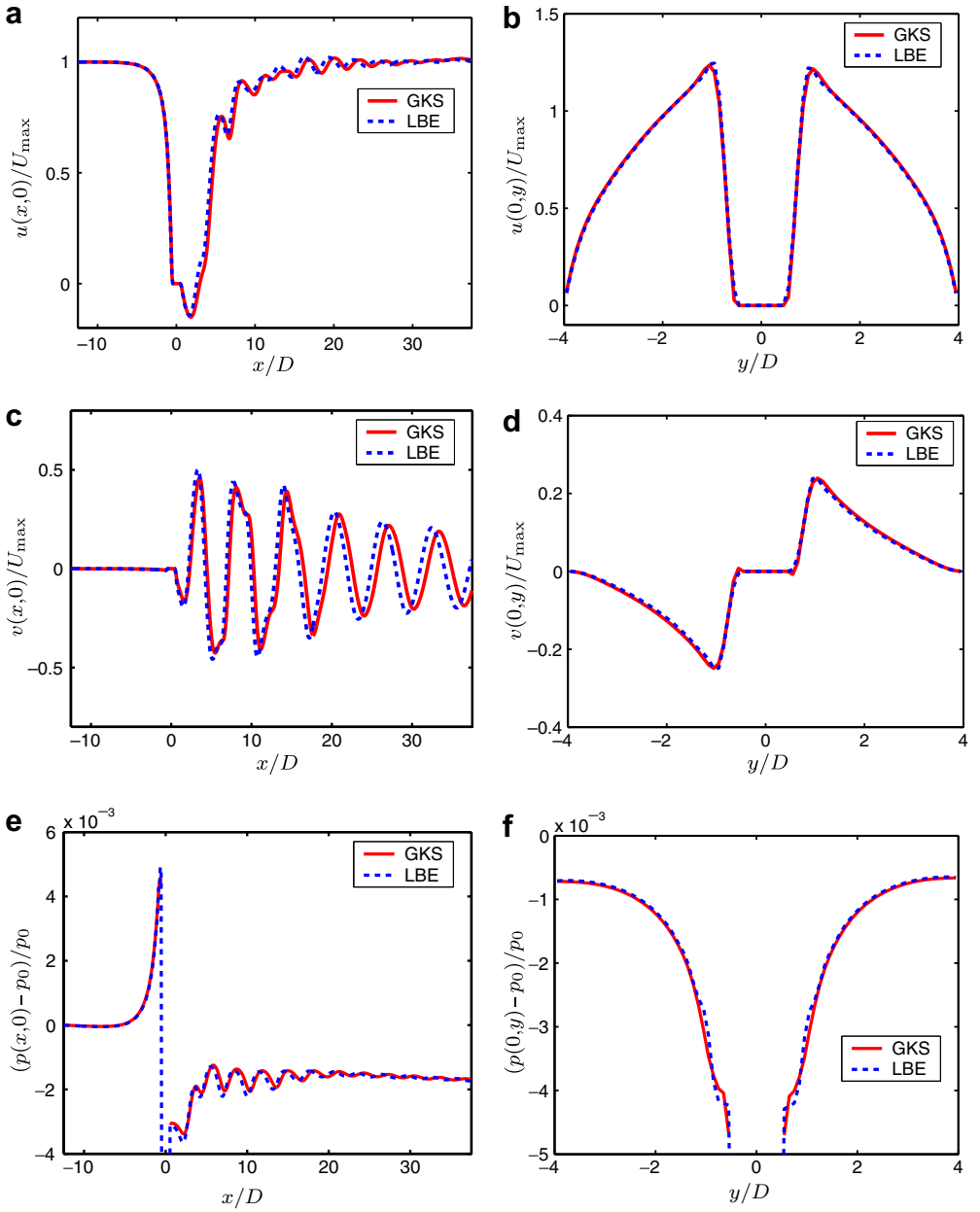

Fig. 10. Similar to Fig. 4. Velocity profiles at $Re = 100$ with a mesh size of 501×81 (coarse mesh): (a) $u(x,0)$; (b) $u(0,y)$; (c) $v(x,0)$; (d) $v(0,y)$; (e) $(p(x,0)-p_0)/p_0$; (f) $(p(0,y)-p_0)/p_0$.

While the LBE and GKS methods presented in this work are explicit time matching schemes, we would like to point out that various numerical techniques can be applied in the future to accelerate the convergence process for both the LBE and GKS methods. These techniques include multigrid method [57–59], pre-conditioning [60], LU-SGS methods [61], and other implicit time-stepping techniques.

4.2. Unsteady flows

As the Reynolds number increases to the range of $60 < Re \leqslant 300$, the recirculating wake behind the block will become unstable, and the two alternating vortices will shed from the square block. As a result, the flow becomes unsteady and will finally settle to a periodic pattern. The characteristics of this periodic flow can be measured by the mean and variation of the drag coefficient, $\overline{C}_{\mathrm{D}}$ and $\Delta C_{\mathrm{D}} = (C_{\mathrm{D}}^{\max} - C_{D}^{\min})$, the variation of the lift coefficient $\Delta C_{\mathrm{L}} = (C_{\mathrm{L}}^{\max} - C_{\mathrm{L}}^{\min})$, and the Strouhal number $St = f_{\mathrm{s}} D/U_{\max}$, where f_{s} is the vortex shedding frequency.

We first compare the velocity profiles predicted by the LBE and GKS for $Re = 100$ on the coarse mesh. Similar to Fig. 4, Fig. 10 shows various instantaneous velocity profiles with the coarse mesh (501×81) at the time when the lift coefficient just crosses 0 from the bellow. Overall the LBE and GKS results are in agreement with each other: The L^2-norm difference of the velocity fields obtained by the LBE and GKS with the coarse mesh is about 9.3%. However, small discrepancies observed in the velocity profiles along the channel center (Fig. 10a and c) indicates that the oscillating frequency of the GKS result is lower than that of the LBE. This discrepancy in the oscillating frequency is reduced with the fine mesh of 1001×161. The L^2-norm difference of the velocity fields reduces to about 3.1% with the fine mesh. This indicates that the numerical dissipation in the LBE and GKS methods is rather different, and the difference diminishes as the grid refines.

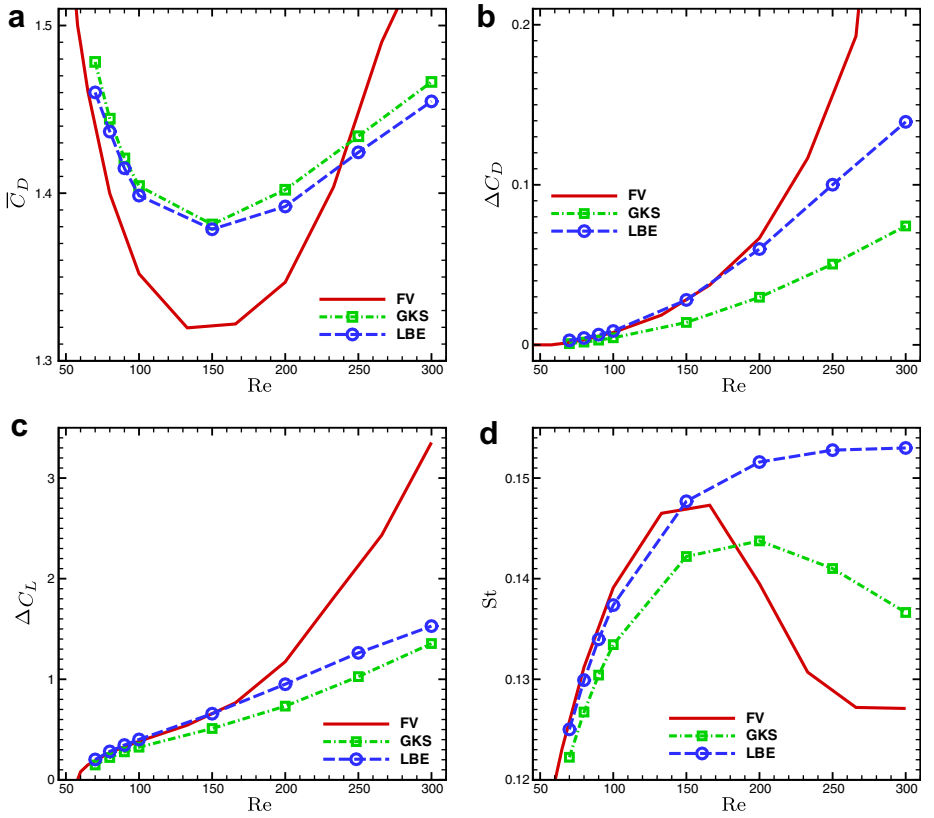

Fig. 11. The Reynolds number dependence of (a) the mean drag coefficient $\overline{C}_{\mathrm{D}}$, (b) the variation of the drag coefficient $\Delta\overline{C}_{\mathrm{D}}$, (c) the variation of the lift coefficient ΔC_{L}, and (d) the Strouhal number St, with a coarse mesh of 501×81. The results obtained a finite-volume (FV) method is from Ref. [32].

To further resolve the discrepancy between the LBE and GKS results, we compare both LBE and GKS with well established finite-volume (FV) data [32]. The FV simulations use a nonuniform mesh of 560×340, with 100 control volumes (CV) around the block, and the chord length of the smallest CV is $0.01D$. Fig. 11 compares the LBE and GKS results of $\overline{C}_D$, ΔC_D, ΔC_L, and St obtained with the coarse mesh (501×81) to the FV results for $60 \leqslant Re \leqslant 300$. For $\overline{C}_D$ shown in Fig. 11a, the LBE and GKS results agree well with each other, but both of them differ considerably from the FV data when $Re > 100$. Both the LBE and GKS results predict a minimum of $\overline{C}_D$ at $Re \approx 150$, consistent with the FV result. The variation of the drag coefficient, ΔC_D, is shown in Fig. 11b The LBE and GKS results agree reasonably well with the FV data up to $Re \approx 150$, and the LBE results are closer to the FV ones when $Re \leqslant 200$. Similar observations can be made for ΔC_L, as shown in Fig. 11c. Furthermore, the FV results indicate that ΔC_L is a nonlinear function of Re when $Re > 150$, but nonlinearity in either the LBE or GKS results, if any, is rather weak. We also note that the LBE results of $\overline{C}_D$, ΔC_D and ΔC_L are consistently larger than that of the GKS.

Fig. 11d shows the Strouhal number St as a function of the Reynolds number. The value of St is measured from the time history of the lift coefficient C_L. Both the LBE and GKS results agree reasonably well with the FV results when $Re \leqslant 100$. The LBE results fail to predict the local maximum of St at $Re \approx 150$, while the GKS results over-predict the maximum at $Re \approx 200$. Also, St obtained by the LBE is always slightly larger than that obtained by the GKS method.

The results of Fig. 11 indicates that, with a coarse mesh of 501×81, both the LBE and GKS can yield quantitative results up to $Re \approx 100$ reasonably well. When $Re > 200$, both the LBE and GKS methods with the coarse mesh of 501×81 cannot capture flow behavior quantitatively. We note that, with a uniform mesh

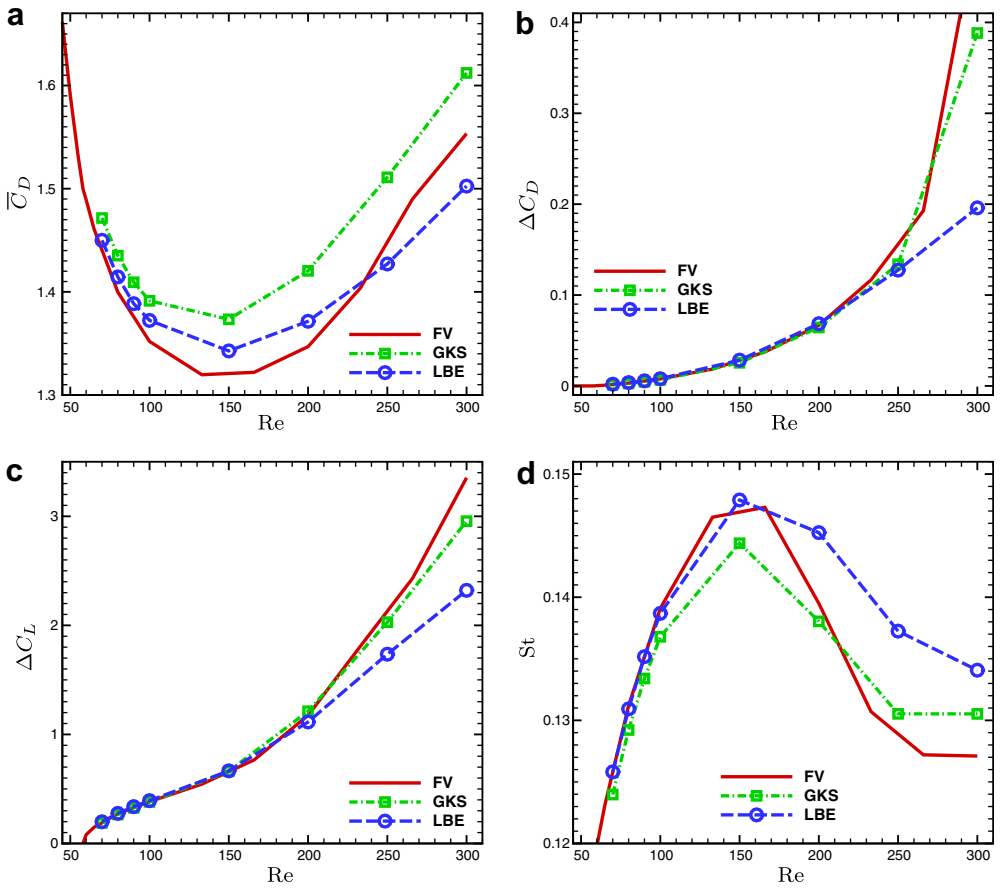

Fig. 12. Same as Fig. 11, but on the fine mesh of 1001×161.

of 501×81, the block is discretized with only 10 cells of a grid size $0.1D$. This is 10 times coarser that the mesh used in the FV simulations [32]. To resolve the discrepancies between the LBE and GKS results and the FV results, we use a finer mesh of 1001×161 to repeat the calculations, and the results are shown in Fig. 12.

Compared to Fig. 11, the results of Fig. 12 shows considerable improvement with the fine mesh of 1001×161, although this finer mesh is still five times coarser around the square block than the one used in the FV simulations [32]. Quantitatively, the LBE and GKS results agree with the FV results much better than the coarser mesh results. The values of $\overline{C}_D$, ΔC_D, ΔC_L and St are in better agreement with the FV data for both LBE and GKS methods up to $Re = 300$, as shown in Fig. 12. Specifically, the nonlinearity of ΔC_L is clearly seen in both the LBE and GKS results. In addition, both the LBE and GKS results predict a local maximum in St, consistent with the FV prediction. We note that, with the finer mesh of 1001×161, the LBE results seem to agree slightly better with the FV results in the lower range of Re ($Re \leqslant 100$), while the GKS results seem to be slightly better in the higher range of Re ($Re \geqslant 250$).

Fig. 13 shows the convergence of the Strouhal number St and the normalized pressure $\bar{p} = (p - p_0)/p_0$ at $Re = 100.0$ and $Ma = 0.1$, where p_0 is pressure at the center of the inlet. Clearly, the results demonstrate that both the LBE and GKS are second-order accurate in space for the unsteady case. While the GKS is second-

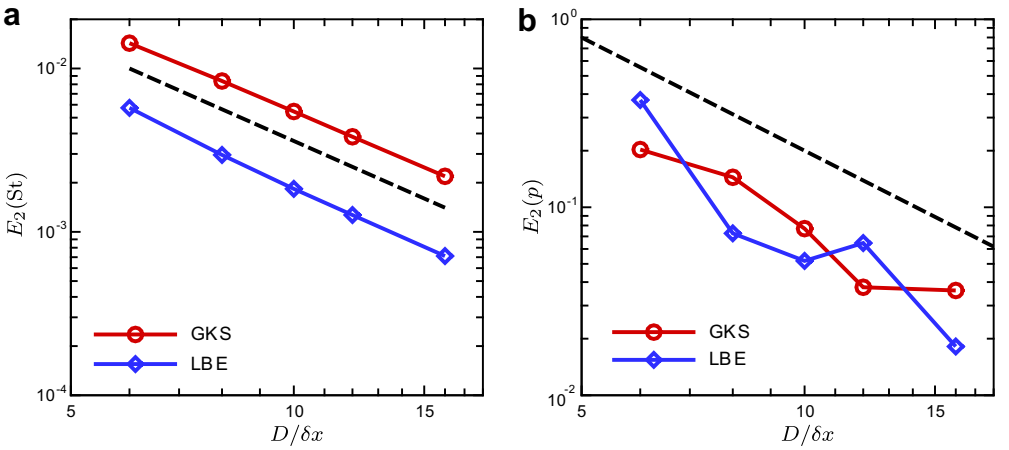

Fig. 13. L^2-norm error of (a) the Strouhal number St and (b) the normalized pressure $\bar{p} = (p - p_0)/p_0$ at the Mach number $Ma = 0.1$ and the Reynolds number $Re = 100.0$, where p_0 is pressure at the center of the inlet. The slop of the dashed lines is -2.

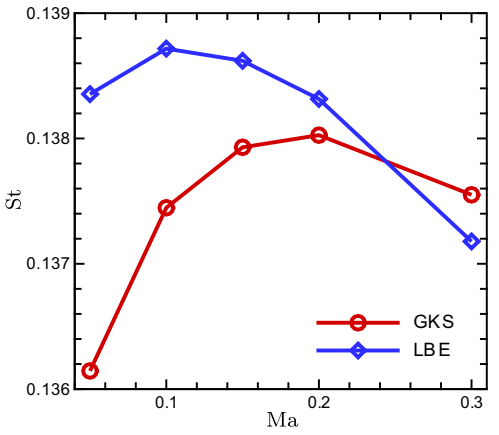

Fig. 14. Mach number dependence of the Strouhal number St, with mesh size 1001×161. The Reynolds number $Re = 100.0$.

order accurate in time [41] and the LBE method has been shown to be only first-order accurate in time asymptotically [39], the results of Fig. 13 clearly indicates that both the LBE and GKS are second-order accurate in time as well, because both grid size and time step have to be refined simultaneously in the simulation. Fig. 14 shows the Mach number dependence of St at $Re = 100.0$. Similar to the steady-state case shown in Fig. 9 for C_D and L_r, St depends on Ma nonlinearly. The variations in St is about 1.0% for both the LBE and GKS methods when $0.05 \leqslant Ma \leqslant 0.3$.

Finally, we investigate the robustness of both methods. With the coarse mesh of 501×81 ($D = 10\delta x$), the LBE code is stable up to $Re \approx 7000$, while the GKS code with the CFL number $\eta = 0.4$ is stable up to $Re \approx 100,000$. The robustness of the GKS method may be in part attributed to the interpolations used in the method and the upwinding nature of the method [55]. This suggests that the GKS has a numerical dissipation which is absent in the LBE method. Thus, the robustness and stability for under-resolved cases are expected [55].

5. Conclusions

In this paper, we conduct a quantitative comparison between two kinetic methods for CFD, i.e. the lattice Boltzmann equation (LBE) and the gas-kinetic scheme (GKS). The comparative study is carried out by simulating the test case of incompressible flow past a square block symmetrically placed in a channel in two dimensions. We investigate the numerical accuracy, computational efficiency and robustness of both methods. Our findings are summarized as follows.

While the spatial discretizations of the LBE and GKS methods are rather different, the former is a finite difference scheme and the latter is a finite-volume one, both methods have the same second-order accuracy in space. Thus, as far as the convergence in space is concerned, they are not expected to behave significantly different from each other for low-Mach number flow calculations for which they are both valid. The LBE and GKS methods yield comparable results as expected, and when sufficient grid resolution is provided, both the LBE and GKS results agree well with existing well-resolved results obtained by other well-established methods. Although it has been shown that the GKS is second-order accurate in time [41] while the LBE is only first-order accurate in time asymptotically [39], we observe that both the LBE and GKS are second-order accurate in time for the unsteady flow calculations.

It should be stressed that the LBE and GKS methods are designed for different flow regions: the former is strictly for near incompressible flows with low-Mach number restriction $Ma < 0.3$, while the latter is designed for fully compressible flows, even though both of them are originated from the linearized Boltzmann equation. The drastic approximations made in deriving the LBE [37,38] make the LBE a very efficient algorithm. While both the LBE and GKS methods are explicit time-matching schemes, the LBE calculation is much simpler and involves less floating point operations (FLOPs) on each node per time step than the GKS method. Consequently, the LBE is about three times faster node-wise per time step than the GKS method. As a results, the LBE is about one order of magnitude faster for 2D steady-state calculations. We should also point out that, while the GKS is not limited to the low Mach number restriction and capable to simulate fully compressible flows, it is not straightforward to extend the LBE for fully compressible flows. There have been various attempts to extend the LBE for compressible flows [62,63], however, they invariably make the LBE much more complicated and yet may not be effective or efficient.

We also note that numerically the GKS method is far more robust than the LBE method in general. With the same grid resolution, the GKS method can reach a Reynold number at least one order of magnitude larger than that the LBE method can, even though the grid resolution is absolutely inadequate to resolve the flow at that high-Reynolds number. This can be attributed to the interpolations used in the GKS method and the upwinding nature of the method, and it is known that interpolations can introduce severe numerical viscosity in small scales [5]. Thus, these two methods should behave differently in small scales close to grid spacing, because of the differences of their numerics.

In conclusion, we found both the LBE and GKS methods are reliable second-order schemes for low-Mach number flows, and the LBE is about 10 and 3 times faster than the GKS for steady and unsteady flow calculations, respectively, while the GKS uses less memory. We also notice that the GKS method is more robust and stable in under-resolved cases due to its numerical viscosity, which is absent in the LBE method.

Acknowledgments

The authors are grateful to Drs. M. Breuer and Th. Zeiser for providing the data in Ref. [32], which are shown in Figs. 11 and 12. Z.L. Guo is supported by the 973 Program (Grant No. 2006CB705804) and the National Natural Science Foundation of China (Grant No. 50606012). L.-S. Luo is supported by the US DOD under AFOSR-MURI project "Hypersonic transition and turbulence with non-equilibrium thermochemistry" (Dr. J. Schmisseur, Program Manager) and by NASA Langley Research Center under a C&I grant through the NIA Cooperative Agreement Grant No. NCC-1-02043. The work of H.W. Liu and K. Xu described in this paper was substantially supported by grants from the Research Grants Council of the Hong Kong Special Administrative Region, China (Project Nos. HKUST6210/05E and 6214/06E).

References

[1] B. Van Leer, Computational fluid dynamics: science or toolbox, in: AIAA Paper 2001-2520, 2001.
[2] M. Karttunen, I. Vattulainen, A. Lukkarinen (Eds.), Novel Methods in Soft Matter Simulations, vol. 640 of Lecture Notes in Physics, Springer, Berlin, 2004.
[3] D. Yu, R. Mei, L.-S. Luo, W. Shyy, Viscous flow computations with the method of lattice Boltzmann equation, Prog. Aerospace Sci. 39 (2003) 329–367.
[4] K. Xu, A gas-kinetic BGK scheme for the Navier–Stokes equations and its connection with artificial dissipation and Godunov method, J. Comput. Phys. 171 (1) (2001) 289–335.
[5] P. Lallemand, L.-S. Luo, Theory of the lattice Boltzmann method: acoustic and thermal properties in two and three dimensions, Phys. Rev. E 68 (2003) 036706.
[6] K. Xu, S.H. Lui, Rayleigh–Bénard simulation using the gas-kinetic Bhatnagar–Gross–Krook scheme in the incompressible limit, Phys. Rev. E 60 (1) (1999) 464–470.
[7] K. Xu, A well-balanced gas-kinetic scheme for the shallow-water equations with source terms, J. Comput. Phys. 178 (2) (2002) 533–562.
[8] X. Shan, H. Chen, Lattice Boltzmann model for simulating flows with multiple phases and components, Phys. Rev. E 47 (1993) 1815–1819.
[9] L.-S. Luo, Unified theory of the lattice Boltzmann models for nonideal gases, Phys. Rev. Lett. 81 (1998) 1618–1621.
[10] L.-S. Luo, Theory of lattice Boltzmann method: lattice Boltzmann models for nonideal gases, Phys. Rev. E 62 (2000) 4982–4996.
[11] Z.L. Guo, T.S. Zhao, Discrete velocity and lattice Boltzmann models for binary mixtures of nonideal fluids, Phys. Rev. E 68 (2003) 035302.
[12] L.-S. Luo, S.S. Girimaji, Lattice Boltzmann model for binary mixtures, Phys. Rev. E 66 (2002) 035301(R).
[13] L.-S. Luo, S.S. Girimaji, Theory of the lattice Boltzmann method: two-fluid model for binary mixtures, Phys. Rev. E 67 (2003) 036302.
[14] P. Asinari, Viscous coupling based lattice Boltzmann model for binary mixtures, Phys. Fluid 17 (6) (2005) 067102.
[15] P. Asinari, L.-S. Luo, A consistent lattice Boltzmann equation with baroclinic coupling for mixtures, J. Comput. Phys. 227 (8) (2008) 3878–3895.
[16] Y.S. Lian, K. Xu, A gas-kinetic scheme for reactive flows, Comput. Fluid 29 (7) (2000) 725–748.
[17] Y.S. Lian, K. Xu, A gas-kinetic scheme for multimaterial flows and its application in chemical reactions, J. Comput. Phys. 163 (2) (2000) 349–375.
[18] P. Dellar, Lattice kinetic schemes for magnetohydrodynamics, J. Comput. Phys. 163 (2002) 95–126.
[19] H.Z. Tang, K. Xu, A high-order gas-kinetic method for multidimensional ideal magneto-hydro-dynamics, J. Comput. Phys. 165 (1) (2000) 69–88.
[20] K. Xu, Gas-kinetic theory-based flux splitting method for ideal magneto-hydro-dynamics, J. Comput. Phys. 153 (2) (1999) 334–352.
[21] Z.L. Guo, T.S. Zhao, Y. Shi, Physical symmetry, spatial accuracy, and relaxation time of the lattice Boltzmann equation for microgas flows, J. Appl. Phys. 99 (2006) 074903.
[22] F. Verhaeghe, L.-S. Luo, B. Blanpain, Lattice Boltzmann modelling of microchannel flow in slip flow regime, Phys. Fluid (2006).
[23] K. Xu, Super-Burnett solutions for Poiseuille flow, Phys. Fluid 15 (2003) 2077–2080.
[24] K. Xu, Z.H. Li, Microchannel flow in the slip regime: gas-kinetic BGK-Burnett solutions, J. Fluid Mech. 513 (2004) 87–110.
[25] K. Xu, X.Y. He, Lattice Boltzmann method and gas-kinetic BGK scheme in the low-Mach number viscous flow simulations, J. Comput. Phys. 190 (1) (2003) 100–117.
[26] P.L. Bhatnagar, E.P. Gross, M. Krook, A model for collision processes in gases. I. Small amplitude processes in charged and neutral one-component systems, Phys. Rev. 94 (1954) 511–525.
[27] Y. Qian, D. d'Humières, P. Lallemand, Lattice BGK models for Navier–Stokes equation, Europhys. Lett. 17 (1992) 479–484.
[28] H. Chen, S. Chen, H.W. Matthaeus, Recovery of the Navier–Stokes equations using a lattice-gas Boltzmann method, Phys. Rev. A 45 (1992) R5339–R5342.
[29] I. Ginzburg, D. d'Humières, Multireflection boundary conditions for lattice Boltzmann models, Phys. Rev. E 68 (2003) 066614.

[30] C. Pan, L.-S. Luo, C.T. Miller, An evaluation of lattice Boltzmann schemes for porous medium flow simulation, Comput. Fluid 35 (8/9) (2006) 898–909.
[31] D. d'Humières, Generalized lattice-Boltzmann equations, in: B.D. Shizgal, D.P. Weave (Eds.), Rarefied Gas Dynamics: Theory and Simulations, vol. 159 of Prog. Astronaut. Aeronaut., AIAA, Washington, DC, 1992, pp. 450–458.
[32] M. Breuer, J. Bernsdorf, T. Zeiser, F. Durst, Accurate computations of the laminar flow past a square cylinder based on two different methods: lattice-Boltzmann and finite-volume, Int. J. Heat Fluid Flow 21 (2000) 186–196.
[33] S. Chapman, T.G. Cowling, The Mathematical Theory of Non-Uniform Gases, third ed., Cambridge University Press, Cambridge, UK, 1970.
[34] S. Harris, An Introduction to the Theory of the Boltzmann Equation, Dover, Mineola, NY, 2004.
[35] H. Grad, Principles of the kinetic theory of gases, in: S. Flügge (Ed.), Handbuch der Physik, Springer, Berlin, 1958, pp. 204–294.
[36] E.P. Gross, E.A. Jackson, Kinetic models and the linearized Boltzmann equation, Phys. Fluid 2 (4) (1959) 432–441.
[37] X. He, L.-S. Luo, A priori derivation of the lattice Boltzmann equation, Phys. Rev. E 55 (1997) R6333–R6336.
[38] X. He, L.-S. Luo, Theory of lattice Boltzmann method: from the Boltzmann equation to the lattice Boltzmann equation, Phys. Rev. E 56 (1997) 6811–6817.
[39] M. Junk, A. Klar, L.-S. Luo, Asymptotic analysis of the lattice Boltzmann equation, J. Comput. Phys. 210 (2) (2005) 676–704.
[40] J.C. Tannehill, D.A. Anderson, R.H. Pletcher, Computational Fluid Mechanics and Heat Transfer, second ed., Taylor & Francis, London, UK, 1997.
[41] T. Ohwada, On the construction of kinetic schemes, J. Comput. Phys. 177 (2002) 156–175.
[42] P. Lallemand, L.-S. Luo, Theory of the lattice Boltzmann method: dispersion, dissipation, isotropy, Galilean invariance, and stability, Phys. Rev. E 61 (2000) 6546–6562.
[43] D. d'Humières, I. Ginzburg, M. Krafczyk, P. Lallemand, L.-S. Luo, Multiple-relaxation-time lattice Boltzmann models in three-dimensions, Philos. Trans. R. Soc. Lond. A 360 (2002) 437–451.
[44] R. Rubinstein, L.-S. Luo, Theory of the lattice Boltzmann equation: symmetry properties of discrete velocity sets, Phys. Rev. E (2008), in press.
[45] T. Ohwada, K. Xu, The kinetic scheme for the full-Burnett equations, J. Comput. Phys. 201 (2004) 315–332.
[46] R.W. Davis, E.F. Moore, L.P. Purtell, A numerical-experimental study of confined flow around rectangular cylinders, Phys. Fluid A 27 (1984) 46–59.
[47] A. Mukhopadhyay, G. Biswas, T. Sundararajan, Numerical investigation of confined wakes behind a square cylinder in a channel, Int. J. Numer. Method Fluid 14 (1992) 1473–1484.
[48] H. Suzuki, Y. Inoue, T. Nishimura, F. Fukutani, K. Suzuki, Unsteady flow in a channel obstructed by a square rod (crisscross motion of vortex), Int. J. Heat Fluid Flow 14 (1993) 2–9.
[49] A.J.C. Ladd, Numerical simulations of particulate suspensions via a discretized Boltzmann equation. Part 1. Theoretical foundation, J. Fluid Mech. 271 (1994) 285–309.
[50] A.J.C. Ladd, Numerical simulations of particulate suspensions via a discretized Boltzmann equation. Part 2. Numerical results, J. Fluid Mech. 271 (1994) 311–339.
[51] A.J.C. Ladd, R. Verberg, Lattice Boltzmann simulations of particle–fluid suspensions, J. Stat. Phys. 104 (2001) 1191–1251.
[52] I. Ginzbourg, P.M. Adler, Boundary flow condition analysis for the three-dimensional lattice Boltzmann model, J. Phys. II 4 (1994) 191–214.
[53] M. Bouzidi, M. Firdaouss, P. Lallemand, Momentum transfer of Boltzmann-lattice fluid with boundaries, Phys. Fluid 13 (2001) 3452–3459.
[54] R. Mei, D. Yu, W. Shyy, L.-S. Luo, Force evaluation in the lattice Boltzmann method involving curved geometry, Phys. Rev. E 65 (2002) 041203.
[55] M. Torrilhon, K. Xu, Stability and consistency of kinetic upwinding for advection–diffussion equations, IMA J. Numer. Anal. 26 (4) (2006) 686–722.
[56] X. He, L.-S. Luo, Lattice Boltzmann model for the incompressible Navier–Stokes equation, J. Stat. Phys. 88 (1997) 927–944.
[57] J. Tölke, M. Krafczyk, M. Schulz, E. Rank, R. Berrios, Implicit discretization and nonuniform mesh refinement approaches for FD discretizations of LBGK models, Int. J. Mod. Phys. C 9 (1998) 1143–1157.
[58] J. Tölke, M. Krafczyk, E. Rank, A multigrid solver for the discrete Boltzmann equation, J. Stat. Phys. 107 (2002) 573–591.
[59] D.J. Mavriplis, Multigrid solution of the steady-state lattice Boltzmann equation, Comput. Fluid 35 (2006) 793–804.
[60] Z.L. Guo, T.S. Zhao, Y. Shi, Preconditioned lattice-Boltzmann method for steady flows, Phys. Rev. E 70 (2004) 066706.
[61] K. Xu, M.L. Mao, L. Tang, A multidimensional gas-kinetic BGK scheme for hypersonic viscous flow, J. Comput. Phys. 203 (2) (2005) 405–421.
[62] C. Sun, Simulations of compressible flows with strong shocks by an adaptive lattice Boltzmann model, J. Comput. Phys. 161 (2000) 70–84.
[63] C. Sun, Adaptive lattice Boltzmann model for compressible flows: viscous and conductive properties, Phys. Rev. E 61 (2000) 2645–2653.